

## Coupled Ocean–Atmosphere–Ice Response to Variations in the Southern Annular Mode

ALEXANDER SEN GUPTA AND MATTHEW H. ENGLAND

*Centre for Environmental Modelling and Prediction, School of Mathematics, University of New South Wales, Sydney, New South Wales, Australia*

(Manuscript received 2 August 2005, in final form 30 November 2005)

### ABSTRACT

The coupled ocean–atmosphere–ice response to variations in the Southern Annular Mode (SAM) is examined in the National Center for Atmospheric Research (NCAR) Community Coupled Climate Model (version 2). The model shows considerable skill in capturing the predominantly zonally symmetric SAM while regional deviations between model and observation SAM winds go a long way in explaining the generally small differences between simulated and observed SAM responses in the ocean and sea ice systems. Vacillations in the position and strength of the circumpolar winds and the ensuing variations in advection of heat and moisture result in a dynamic and thermodynamic forcing of the ocean and sea ice. Both meridional and zonal components of ocean circulation are modified through Ekman transport, which in turn leads to anomalous surface convergences and divergences that strongly affect the meridional overturning circulation and potentially the pathways of intermediate water ventilation. A heat budget analysis demonstrates a conspiring of oceanic meridional heat advection, surface heat fluxes, and changes in mixed layer depth, which acts in phase to imprint a strong circumpolar SAM signature onto sea surface temperatures (SSTs), while other oceanic processes, including vertical advection, are shown to play only a minor role in contrast to previous suggestions. Lagged correlations show that although the SAM is mainly controlled by internal atmospheric mechanisms, the thermal inertia of the ocean reimprints the SAM signature back onto surface air temperatures (SATs) on time scales longer than the initial atmospheric signal. Sea ice variability is well explained by a combination of atmospheric and oceanic dynamic and thermodynamic forcing, and by an albedo feedback mechanism that allows ice extent anomalies to persist for many months. Nonzonally symmetric components of the SAM winds, particularly in the region surrounding the Antarctic Peninsula, have important effects for other climate variables.

### 1. Introduction

Large differences in the radiation budget between the Tropics and the high albedo Poles mean that the largest global temperature gradients occur at midlatitudes. In the troposphere thermal wind balance implies that these meridional temperature gradients manifest themselves as a geostrophic westerly wind, which extends from the surface and reaches maximum strength in the upper troposphere as the subtropical jet. The strong flow, together with the large tropospheric temperature gradient, provides the energy for baroclinic instability and the formation of transient eddies. These eddies are associated with a large degree of variability

and have the ability to interact with and feedback onto the mean flow. The dominant mode of variability associated with the midlatitude westerlies is characterized by swings between a stronger and poleward-shifted or weaker and equatorward-shifted flow. In terms of anomalies, this translates to vacillations in a zonally symmetric, meridionally varying dipole pattern centered about the climatological mean flow. The patterns are equivalent barotropic, extending through large proportions of the atmosphere. This mode of variability exists in the high latitudes of both hemispheres. However the zonal symmetry is particularly evident in the Southern Hemisphere where the Southern Ocean provides a longitudinally uninterrupted area with few land masses breaking the symmetry. The variability shows significant strength spanning monthly to interannual time scales, although there is still a debate over its dominance at low frequencies when the influence of the Antarctic “Circumpolar Wave” becomes important

---

*Corresponding author address:* Alex Sen Gupta, Centre for Environmental Modelling and Prediction, School of Mathematics, University of New South Wales, Sydney, NSW, Australia.  
E-mail: alexg@maths.unsw.edu.au

(White 2004; Visbeck and Hall 2004). In the Southern Hemisphere, this Southern Annular Mode (SAM) of variability (also referred to as the high-latitude mode, the Antarctic Oscillation, and the zonal index) is manifest in many atmospheric variables including geopotential height, sea level pressure, air temperature, and storm track activity (Brahmananda Rao et al. 2003), and signatures of the mode are also evident in ocean and sea ice variability.

Observational (e.g., Karoly 1990; Hartmann and Lo 1998; Lorenz and Hartmann 2001) and model (e.g., Robinson 1991; Limpasuvan and Hartmann 2000; Codron 2005) studies suggest that the persistence and dominance of the SAM can be explained in terms of a positive feedback between the zonal winds (in particular near the region of the eddy-driven midlatitude jet) and fluxes of transient eddy momentum. In an analysis of observed zonally averaged momentum balance, for example, Lorenz and Hartmann (2001) show that, in addition to a high correlation between eddy momentum flux and zonal wind anomalies when eddy activity leads by a few days, there is also a significant positive correlation with eddy activity lagging by up to two weeks. By comparing to a simple linear model, the authors demonstrate that this represents a positive feedback (with effects reaching beyond the eddy decorrelation time scale) whereby a component of these eddies—the high-frequency synoptic eddies—is organized by the eddy-generated anomalous wind such that they have a large feedback onto the zonal winds. This significantly increases the total variability of the zonal winds, particularly at low frequencies, and allows the anomalous winds to persist over longer periods. Recently Codron (2005) described similar mechanisms driving SAM variability in a series of (constant forcing) atmospheric general circulation model (AGCM) runs. His analysis of both the AGCM and reanalysis observations shows that the high-frequency eddy–wind feedback mechanism holds for all longitudes and for different positions of the maximum winds occurring at different seasons and at the extremes of the El Niño–Southern Oscillation (ENSO) cycle.

The ability to realistically capture SAM variability in uncoupled AGCM integrations, under both idealized and realistically varying ice/ocean forcing, indicates that it is internal atmospheric physics that maintains this mode—without the need for any particular variability in the external forcing. However, there is evidence that the SAM, in particular its temporal evolution, is sensitive to external forcing. Zhou and Yu (2004), for example, show that there is a small but significant predictability to the observed SAM based on ensemble AGCM integrations where ocean SST is pre-

scribed from observations. Carril and Navarra (2001) also show a modulation of the SAM by extratropical forcing during summer months. Watterson (2000) uses an idealized model to explain results from a coupled climate model and finds improved agreement with the inclusion of a feedback term from the ocean to the atmosphere. Despite these studies it remains unclear to what extent the SAM is affected by ocean–atmosphere coupling, both in generating its low-frequency variability and in modulating its amplitude.

The influence of the SAM extends over the midlatitude continental land masses. Anomalous precipitation patterns also tend to follow the meridional dipole pattern. Boer et al. (2001), for example, find that moisture advection associated with low-level meridional winds and anomalous eddy transport causes decreased (increased) precipitation at middle (high) latitudes during positive SAM phases. This is consistent with the simulated rainfall response of Cai and Watterson (2002), who go on to show the importance of this mode in increasing (decreasing) rainfall over eastern (western) South Australia through an increase (decrease) in moisture advection from the adjacent ocean region. Silvestri and Vera (2003) find evidence of regional effects of the SAM on precipitation over southeastern South America with significant SAM-related precipitation anomalies of opposite polarities in July–August and November–December. They also find a modulation of the ENSO-related precipitation by the SAM. The Southern Annular Mode has also been linked to variations in mid- and high-latitude primary production. Using satellite estimates of chlorophyll Lovenduski and Gruber (2005) suggest that high-latitude levels are sensitive to changes in the upwelling of iron, while midlatitude production is affected by changes in light limitation due to variations in mixed layer depths.

An understanding of the SAM thus has important environmental and economic implications. This is particularly true as in recent decades there appears to have been a significant trend in the Southern Hemisphere extratropical climate with a large component of this trend being explained by a shift toward a more positive SAM phase (e.g., Thompson and Wallace 2000; Kushner et al. 2001; Thompson and Solomon 2002; Marshall et al. 2004). Observational and modeling studies have demonstrated that these trends are consistent with a combination of recent stratospheric ozone depletion (e.g., Thompson and Wallace 2000; Sexton 2001; Gillett and Thompson 2003) and enhanced greenhouse gas forcing (e.g., Fyfe et al. 1999; Cai et al. 2003).

The barotropic nature of the SAM implies a strong surface signature. It follows that the SAM should play an important role in forcing the ocean and ice, whose

variability in the extratropics is largely due to the integrated effect of atmospheric variability. Significant changes in surface winds of the subpolar westerlies directly affect both Ekman flow and, in conjunction with altered air temperature and moisture distributions, air-sea fluxes of heat and freshwater. SAM-related cloud cover anomalies can also affect radiation fluxes to the ocean. Various observational studies (Mo 2000; Liu et al. 2004) and coupled model simulations (Watterson 2000; Hall and Visbeck 2002; Lefebvre et al. 2004) have shown that there is indeed a significant ocean/ice response to the SAM.

This study examines the effect of the SAM on a number of atmospheric, oceanic, and sea ice characteristics, in particular attempting to explain the coupling between these properties through a detailed heat budget and regression analysis. We employ output from a fully coupled state-of-the-art ocean-atmosphere-ice-land model described in section 2a. Where possible, we compare our results with available observational reanalysis data (described in section 2b). Section 3 provides a brief overview of the dominant modes of Southern Hemisphere extratropical variability. The atmospheric response of sea level pressure (SLP), wind, surface air temperature, and precipitation to SAM (section 4a) shows a striking similarity to observations. In the ocean (section 4b) both dynamic and thermodynamic responses to the atmospheric forcing are seen in the SST, surface currents, and also in the deeper circulation. The sea ice response to the SAM (section 4c) also shows similarities to observations consistent with the atmosphere and ocean forcing. Section 5 provides a discussion and summary of the SAM response in the coupled ocean-atmosphere-ice system.

## 2. Model and reanalysis data description

### a. The CCSM coupled model

Climate data in the high-latitude Southern Hemisphere are relatively sparse, and high-quality time series suitable for examining both variability and recent trends generally only cover the last few decades. As a result, many conclusions drawn from these data are often uncertain and generally marginal in terms of statistical significance. Model output of much higher resolution and covering substantially longer time scales can be used to complement observations and to help elucidate the governing physics of the observed climate variability. This study analyzes model output from the last 200 years of a 1350-yr integration of the Community Climate System Model version 2 (CCSM2) developed by the National Center for Atmospheric Research (NCAR). This control run is integrated with constant

1990 level greenhouse forcing. There are no flux corrections for the air-sea exchange of heat, freshwater, and momentum, resulting in a more realistic representation of climate variability. The CCSM2 has a modular structure controlled by a coupler, which facilitates the interpolation and transfer of surface fluxes and synchronizes the component models representing the atmosphere, ocean, land, and sea ice. Information regarding the submodels is given in Table 1. A detailed description of the CCSM2 together with an analysis of the control-run mean state and interannual variability can be found in Kiehl and Gent (2004). The CCSM2 variability in the Tropics is weaker than observed with a sharp 2–3-yr spectral peak in ENSO activity, as opposed to observations which show a broad 3–7-yr peak (Kiehl and Gent 2004). Northern extratropical variability is, however, well simulated, with CCSM2 realistically capturing the North Atlantic Oscillation (NAO) spatial pattern (Kiehl and Gent 2004). Variability in Arctic sea ice and the surrounding ocean area is also found to be well represented (Holland 2003). In a study focused on the Antarctic Dipole, Holland et al. (2005) provide a brief description of the CCSM climate response to the SAM. They show that the leading mode of Southern Hemisphere sea ice variability—the Antarctic Dipole, which is characterized by anomalies of opposite polarity in the Atlantic and Pacific sectors—is realistically simulated, with both the ENSO and the SAM contributing to this pattern. In section 4a, we will analyze the CCSM2 representation of the SAM in greater detail.

### b. Reanalysis observational datasets

The low spatial resolution of high-latitude southern observations has led to the extensive use of reanalysis datasets that assimilate relatively scarce observations into physically consistent, model generated, gridded datasets. A number of these datasets are used here to compare against modeled variability.

The primary “observed” SAM index is formed from SLP from the 40-yr European Centre for Medium-Range Weather Forecasts (ECMWF) Re-Analysis (ERA-40; Table 2). Bromwich and Fogt (2004) show that the ERA-40 SLP is superior to the (National Centers for Environmental Prediction) NCEP–NCAR reanalysis (NNR) in comparisons with mid and high southern latitude station observations after 1978. In addition, Marshall (2003) finds that, compared to the NNR, the ERA-40 SLP also provides a superior representation of high-latitude Southern Hemisphere variability after 1973. In particular, the NNR exaggerates (by a factor of 2) the recent trend in the SAM index derived from station data. Surface wind, cloud cover,

TABLE 1. Details of the CCSM2 submodels. The studies describing the relevant model physics are noted.

| Component  | Model   | Resolution   | Improved physics  |
|------------|---|--|---|
| Ocean      | Parallel Ocean Program<br>(from the Los Alamos National Laboratory) | ( $1^{\circ}$ longitude $\times 3^{\circ}$ latitude); 40 vertical levels (approximately 10-m resolution in the top 100 m increasing monotonically to 250 m at depth) | Anisotropic horizontal mixing with spatially varying coefficients (Smith and McWilliams 2003)<br>K-profile parameterization of vertical mixing (Large et al. 1994)<br>GM parameterization of eddy mixing (Gent and McWilliams 1990)<br>Accurate equation of state (McDougall et al. 2003) |
| Atmosphere | Community Atmosphere Model, v2.0                                    | T42 ( $\sim 2.8^{\circ} \times 2.8^{\circ}$ ); 26 vertical levels; hybrid sigma-pressure coordinate system from surface to $\sim 3.5$ mb                             | Prognostic scheme for total cloud condensate (Rasch and Kristjansson 1998)<br>New cloud overlap scheme (Collins 2001)<br>Improved cloud water emissivity/absorptivity scheme (Collins et al. 2002)  |
| Land       | Community Land Model, v2  | Horizontal—same as atmospheric grid; 10-layer soil model   | 5 basic land types with further refinement of vegetation types<br>10-layer soil temperature/water model<br>Multilayer snowpack model<br>State-of-the-art river runoff scheme (Branstetter and Erickson 2003)  |
| Sea ice    | Community Sea Ice Model, v4   | Horizontal—same as oceanic grid; 5 thickness categories  | Elastic-viscous-plastic (EVP) dynamics scheme (Hunke and Dukowicz 1997)<br>Subgrid-scale ice thickness distribution (Bitz et al. 2001)<br>Energy-conserving thermodynamics (Bitz and Lipscomb 1999)   |

TABLE 2. Details of reanalysis datasets.

| Property                                   | Dataset  | Description   | Reference  |
|--|--|---|--|
| SLP surface wind precipitation cloud cover | ERA-40   | $2.5^{\circ}$ monthly data from 1958  | (Gibson et al. 1996)   |
| SST  | NOAA Optimum Interpolation SST V2 reanalysis provided by the NOAA–CIRSES (Cooperative Institute for Research in Environmental Sciences) Climate Diagnostics Center (Boulder, CO) from their Web site ( <a href="http://www.cdc.noaa.gov/">http://www.cdc.noaa.gov/</a> ) | $1^{\circ}$ monthly data from 1982. Incorporates an improved simulation of SST observations from sea ice data following a technique developed at the U.K. Met Office, reducing higher-latitude biases in the optimum interpolation SST  | (Reynolds et al. 2002)   |
| SAT  | NNR  | $2.5^{\circ}$ monthly data from 6 hourly records from 1948  | (Kalnay et al. 1996)   |
| Surface current                            | University of Maryland SODA  | $0.5^{\circ}$ monthly data from 1958 (to complement ERA-40). Assimilated: historical archive of hydrographic profiles, ship intake measurements, moored hydrographic observations, remotely sensed SST, and sea level. Forecast model: Parallel Ocean Program ( $0.25^{\circ} \times 0.4^{\circ} \times 40$ -level) | (Carton et al. 2000; J. A. Carton and B. Giese 2005, personal communication) |
| Sea ice cover                              | Hadley Centre, Met Office HadISST 1.1  | $1^{\circ}$ monthly data from 1870 [replaces the global sea ice and sea surface temperature (GISST)]  | (Rayner et al. 2003)   |

and precipitation are also taken from ERA-40. Additional analysis of the Climate Prediction Center (CPC) Merged Analysis of Precipitation (CMAP) (Arkin and Xie 1996) and Global Precipitation Climatology Project (GPCP) (Adler et al. 2003) datasets found that general precipitation responses were insensitive to the dataset used. Similarly, the cloud response for the International Satellite Cloud Climatology Project (ISCCP) dataset was generally consistent with ERA-40 reanalysis presented below. In the ocean, a comparison between the NOAA and Hadley Centre Sea Ice and SST Dataset (HadISST) sea surface temperature reanalyses shows a robust pattern of response north of the ice margin (figure not shown). Other reanalysis datasets used in this study are detailed in Table 2. Unless otherwise stated, all analyses presented in this paper use data from 1979 onward [1982 in the case of surface air temperature (SAT)] to minimize the effect of less reliable years in the climatological records.

### 3. Dominant modes of extratropical variability in the Southern Hemisphere

Before analyzing the coupled climate response to the SAM, we briefly assess the dominant modes of extratropical variability in the Southern Hemisphere. Figure 1 shows the dominant EOFs (presented as regression maps) of several ocean–atmosphere variables in the NCAR CCSM. The EOFs are calculated from unfiltered data from the last 200 years of the natural variability simulation. Clearly apparent are dominant annular modes of variability in SLP, SST, zonal winds, and zonal and meridional ocean currents. These modes are well separated from subsequent modes in the EOF analysis (Fig. 1). The annular mode accounts for between 15% and 35% of total variability with SLP the most dominant annular property (34.8%). In contrast, a distinct wavenumber-3 pattern is apparent in the meridional wind. This mode is poorly separated from the subsequent mode and is indicative of a propagating signal. Similarly, the mixed layer depth mode does not show an annular pattern and is poorly separated from the subsequent EOF mode. A weak annular signature is seen in the leading EOFs for total precipitation and surface air temperature, although for the latter the pattern is dominated by a signature reminiscent of the Antarctic Dipole, centered over the southeast Pacific and Atlantic Oceans (e.g., Yuan and Martinson 2001). Given a dominant annular mode in SLP, it is not surprising that a leading annular mode appears in zonal winds (via geostrophy) and, in turn, meridional ocean currents (via Ekman transport). Given the strong north–south gradient in SST in the Southern Ocean, the

dominant annular mode of variability in meridional currents will contribute to an annular mode in SST. This mode dominates over other SST modes such as the Antarctic Circumpolar Wave (ACW) in the NCAR CCSM. The annular mode in the zonal ocean currents may also be forced directly by the annular mode in SLP. Namely, the associated zonal wind anomalies drive meridional Ekman transport anomalies that, in turn, act to force a north–south sea level anomaly pattern with annular signature. Geostrophic adjustment could then force an annular mode in zonal ocean currents. This will be assessed in greater detail in section 4b. All properties show generally red spectra (not shown) with little evidence of dominant time scales (except for precipitation, which shows a possible 2-yr intensification, matching the model's dominant ENSO time scale). SST shows the greatest “reddening” with little power at subseasonal time scales. In summary, there is evidence that the well-documented annular mode in SLP (Fig. 1a) is manifest in upper ocean properties, including SST and surface ocean currents. Annular signatures also appear in Southern Hemisphere leading EOF patterns of precipitation and surface air temperature. We now turn our attention to the coupled ocean–atmosphere–ice response to variations in the SAM.

### 4. Climate response to the SAM

The dominance of the SAM throughout the troposphere and across a variety of atmospheric variables has led to a number of essentially equivalent definitions of a SAM index. These include principle component time series associated with the dominant empirical orthogonal function of geopotential height (at a variety of pressures) and SLP, or of zonally averaged wind or angular momentum. Practical indices based on differences between maximum and minimum zonally averaged wind anomalies have also been used. For the following analysis, we use a SLP principle component definition based on data south of 20°S such that the strong influence of tropical variability is avoided. By convention, a positive event corresponds to an anomalously negative (positive) SLP at high (mid) latitudes. For all analyses, long-term monthly climatologies have been subtracted from monthly averaged data to form anomalies. To infer climate responses to the SAM we use lagged regression (and correlation) analysis.

#### a. Atmosphere

Figure 2 shows regressions of simulated (CCSM) and observed (ERA-40) SLP associated with the principle component time series of the dominant SLP EOF

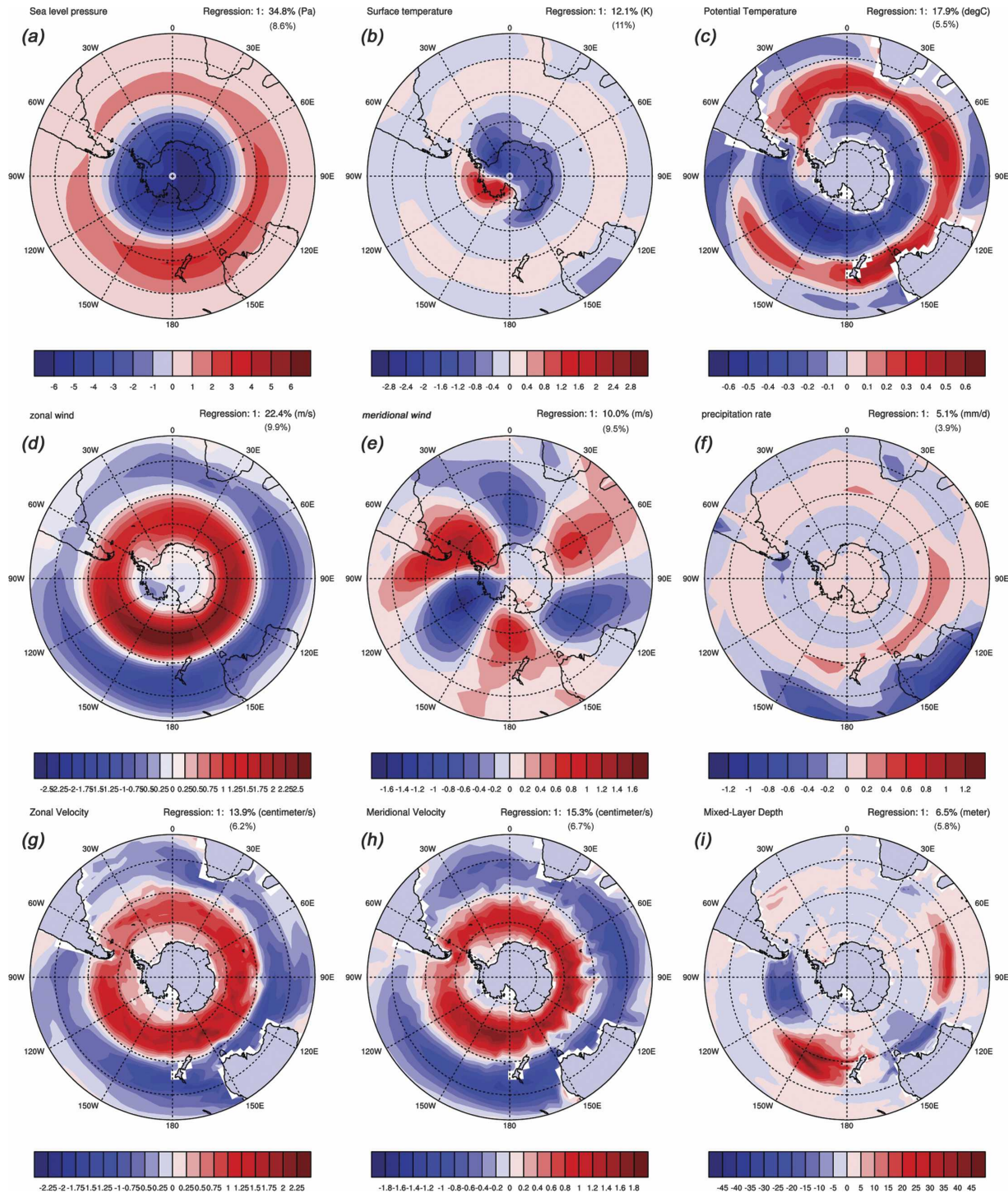


FIG. 1. CCSM dominant EOFs, presented as regression maps (i.e., variable anomaly field regressed on the principle component associated with the dominant EOF of that variable), of (a) SLP, (b) SAT, (c) SST, (d) zonal wind, (e) meridional wind, (f) total precipitation, (g) zonal current, (h) meridional current, and (i) mixed layer depth. EOFs are calculated based on monthly anomalies for data south of 20°S. Anomalies were weighted by the cosine of latitude to ensure that equal areas have equal importance. The percentage of variance explained for the first two dominant modes (second mode in parentheses) is shown for each variable. Using North's rule of thumb (North et al. 1982) with a conservative estimate for the number of independent samples ( $n = 200$ ) SAT, meridional wind, and mixed layer EOFs cannot be considered distinct from their second EOF modes.

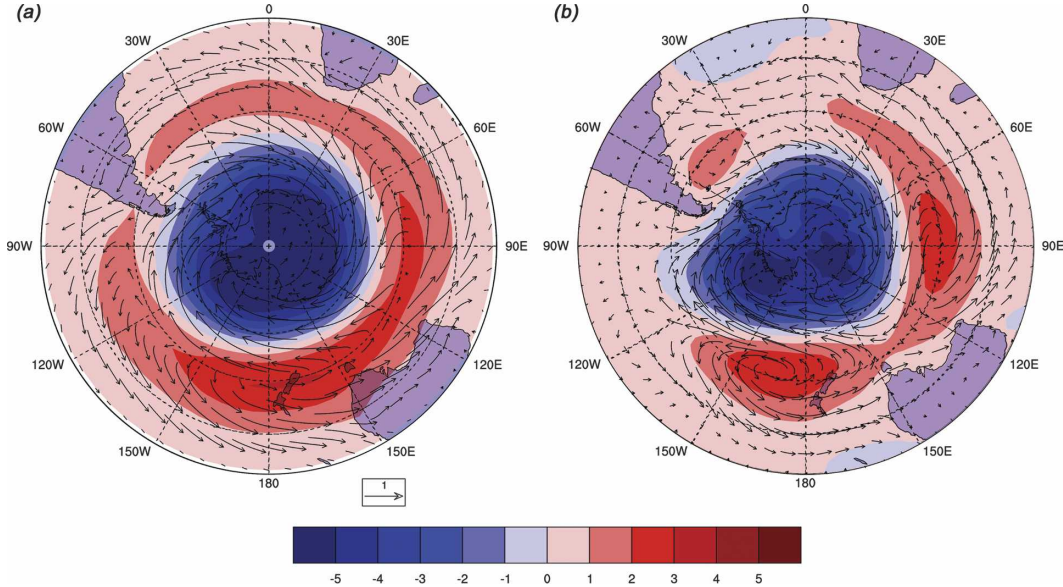


FIG. 2. Regression on the SAM index of (a) CCSM and (b) ECMWF (1979–2002) surface wind vectors ( $1 \text{ m s}^{-1}$  reference vector shown), superimposed on the corresponding SAM SLP signal. The color bar indicates the SLP signal in hPa. All regression maps are formed by taking pointwise linear regressions of an anomaly time series with the standardized SAM index, thus showing the response of a variable to a 1 std dev positive SAM anomaly. Additional plots showing the statistical significance of observed and simulated SLP, surface wind, and other variables can be viewed online (see <http://web.maths.unsw.edu.au/~alexg/>).

(Fig. 1)—our SAM index. This mode explains 24.5% (observed) and 34.5% (modeled) of the total variability and is well separated from subsequent modes (Fig. 1). The next two (degenerate) modes, in both observed and modeled data (not shown), represent a propagating signal that predominantly acts in the Pacific region and has been shown to be strongly related to the ENSO through a teleconnection mediated by Rossby waves traveling from midlatitudes (e.g., Turner 2004). This mode of variability is known as the Pacific–South American Oscillation (PSA).

Both the modeled and observed SLP responses to a one standard deviation positive phase of the SAM (Fig. 2) demonstrate strong zonal symmetry, with negative anomalies over high latitudes south of  $\sim 55^{\circ}\text{S}$  and a circumpolar band of positive anomalies farther north centered at  $\sim 45^{\circ}\text{N}$ . The simulated SAM SLP shows a slightly stronger and more symmetric pattern than observations. For example, the observed SLP response has a large nonsymmetric, low pressure anomaly between  $90^{\circ}$  and  $150^{\circ}\text{W}$ , to the west of Drake Passage (DP), which is much less pronounced in the simulation. It is noted, however, that a similar analysis using SLP reanalysis fields from 1962 to 1982 (not shown) shows this feature to be much reduced. In addition, the second observed SLP EOF (not shown) has its strongest variability in the same region as this negative mode 1

anomaly, so it is conceivable that some leakage is occurring between the first two modes owing to the relatively short length of the observational record. Lachlan-Cope et al. (2001) demonstrates a sensitivity in the strength of this low pressure anomaly to Antarctic topography and the nonaxisymmetric distribution of the Antarctic land mass over the South Pole. In this context, nonrealistic, low-resolution model topography around Antarctica may also contribute to the differences between simulation and observations. Additional analysis from a series of 30-yr subsets of the CCSM time series shows the enhanced zonal symmetry to be a robust feature of the simulated SLP. The strength of the response does, however, vary (variance explained for EOF1 ranges from 27% to 35%), such that the lower range magnitudes are closer to the observations.

The surface winds, although strongly geostrophic, show some deflection off lines of constant pressure as a result of drag forces at the surface (Fig. 2). Simulated westerly wind anomalies extend from the Antarctic margin to  $\sim 45^{\circ}\text{S}$ , and weaker easterly wind anomalies are seen northward of this, as far north as  $\sim 20^{\circ}\text{S}$ . Maximum westerlies (easterlies) occur between  $55^{\circ}$  and  $60^{\circ}\text{S}$  ( $30^{\circ}$  and  $40^{\circ}\text{S}$ ), with largest zonally averaged surface values almost  $2 \text{ m s}^{-1}$  ( $0.8 \text{ m s}^{-1}$ ) near the surface (Fig. 3c). The zonal flow shows an equivalent barotropic structure extending throughout the troposphere

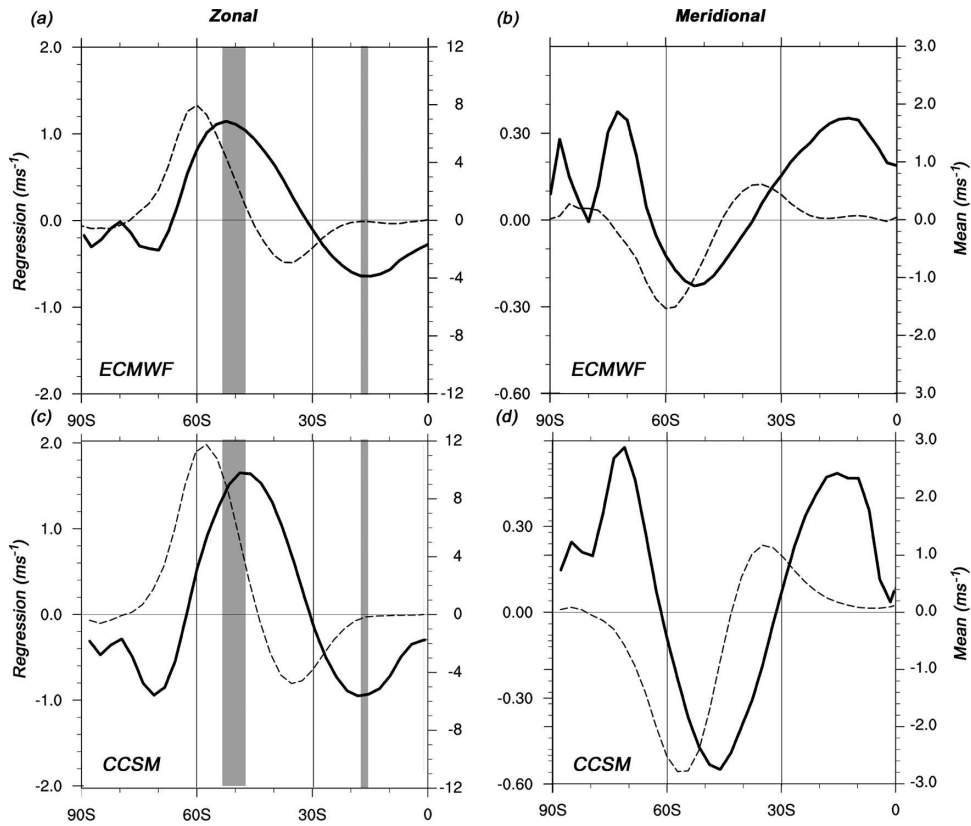


FIG. 3. Surface zonally averaged (a), (c) zonal and (b), (d) meridional winds for the (a), (b) ECMWF reanalysis and (c), (d) CCSM ( $m s^{-1}$ ). Continuous lines and right-hand scales represent annual mean climatology; dotted lines and left-hand scales represent regressions on the corresponding SAM index. Shaded areas in (a), (c) show the range in latitude of maximum and minimum observed climatological winds based on different published climatologies [as presented in P. R. Oke et al. (2005, unpublished manuscript)].

(Fig. 4a) and into the stratosphere and reaching a maximum regression amplitude at  $\sim 200\text{--}250$  mb, flanking the mean-state midlatitude jet stream.

Surface observations of the zonal wind anomalies associated with the SAM show a similar dipole pattern in the zonal mean (Fig. 3a), although the response is somewhat weaker and shifted slightly southward. These differences also apply to the annual mean climatology and thus account for the discrepancy between the position of the simulated and observed zonally averaged response to the SAM. In addition to the purely zonal component of the SAM wind, there is significant regional variation (Fig. 2) that, in conjunction with the surface drag, results in a meridional component to the wind. The surface drag leads to generally poleward surface wind anomalies south of  $\sim 45^{\circ}\text{S}$  and equatorward wind anomalies to the north, with maxima coincident with the surface zonal wind maxima where the effects of friction would be greatest (Fig. 3). The meridional wind strength drops off quickly away from the surface

(Fig. 4b). Overall, the patterns of zonally averaged wind anomalies closely match the results of the low-resolution coupled climate simulations described by Hall and Visbeck (2002). However, the magnitude of their SAM-induced wind anomaly pattern is smaller than both those presented here and those estimated in observations.

Regional departures from the zonally symmetric surface pattern are evident, particularly for the observed winds (Fig. 2b). A notable common regional departure is in the area to the west of the Antarctic Peninsula where winds become more strongly poleward. This meridional intensification is also evident in the simulated wind field response of Lefebvre et al. (2004) but is significantly weaker in the study of Hall and Visbeck (2002), whose coarse-resolution model shows a much more zonally symmetric response. The greater SLP symmetry in the Hall and Visbeck (2002) analysis appears to propagate through to other fields (e.g., zonal wind and zonal and meridional ocean advection). Here

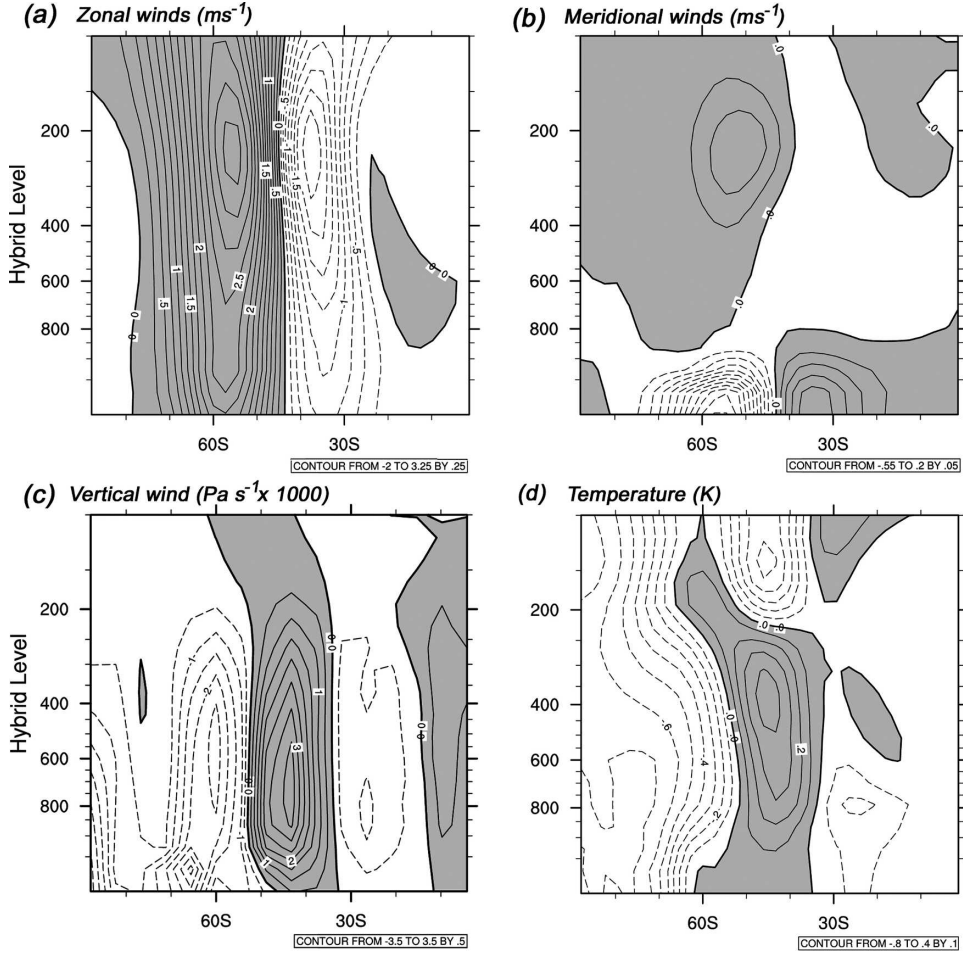


FIG. 4. Regression on the SAM index of zonally averaged (a) zonal ( $\text{m s}^{-1}$ ), (b) meridional ( $\text{m s}^{-1}$ ), and (c) vertical ( $\text{Pa s}^{-1} \times 1000$ ) wind and (d) air temperature (K). All vertical atmospheric sections have been plotted using the CCSM native vertical coordinate system (see online at <http://www.ccsm.ucar.edu/models/atm-cam/index.html>) with sigma coordinates near the surface merging into pressure coordinates at increasing height. This avoids spurious interpolation effects encountered when converting to pressure coordinates.

we find that the zonal differences in wind response translate into important regional differences in other climate variables.

The convergences and divergences associated with the meridional winds result in anomalies of rising and falling air over the Southern Ocean and Antarctic continent, increasing in magnitude from the surface to maxima between 400 and 800 mb. The main rising air anomaly is centered near 60°S and extends southward to the Pole. A weak uplift is also evident, centered between 25° and 30°S. In between, centered at 40°–45°S, the latitude of greatest meridional wind divergence, is an associated region of descending air (Fig. 4c). The surface air temperature response to the SAM is shown in Fig. 5 with simulated zonally averaged temperature profiles shown in Fig. 4d. The zonally aver-

aged response shows a significant cooling above the Antarctic continent (up to  $\sim -0.8^\circ\text{C}$ ) that extends into the stratosphere. At lower latitudes, centered at 40°–50°S, warming occurs to heights of  $\sim 200$  mb above which cooling occurs. These regions coincide with the areas of rising and falling air anomalies (Fig. 4c), and are consistent with adiabatic cooling and warming, respectively. Although a cooling response extends over the bulk of Antarctica in the model, a region over the Antarctic Peninsula and the surrounding ocean shows significant warming (Fig. 5a). The observed surface temperature response (Fig. 5b) shows a similar spatial structure although anomalies are more pronounced than the simulation [both ERA-40 and the NNR (not shown) show almost identical results]. The Antarctic Peninsula response covers a larger domain in the ob-

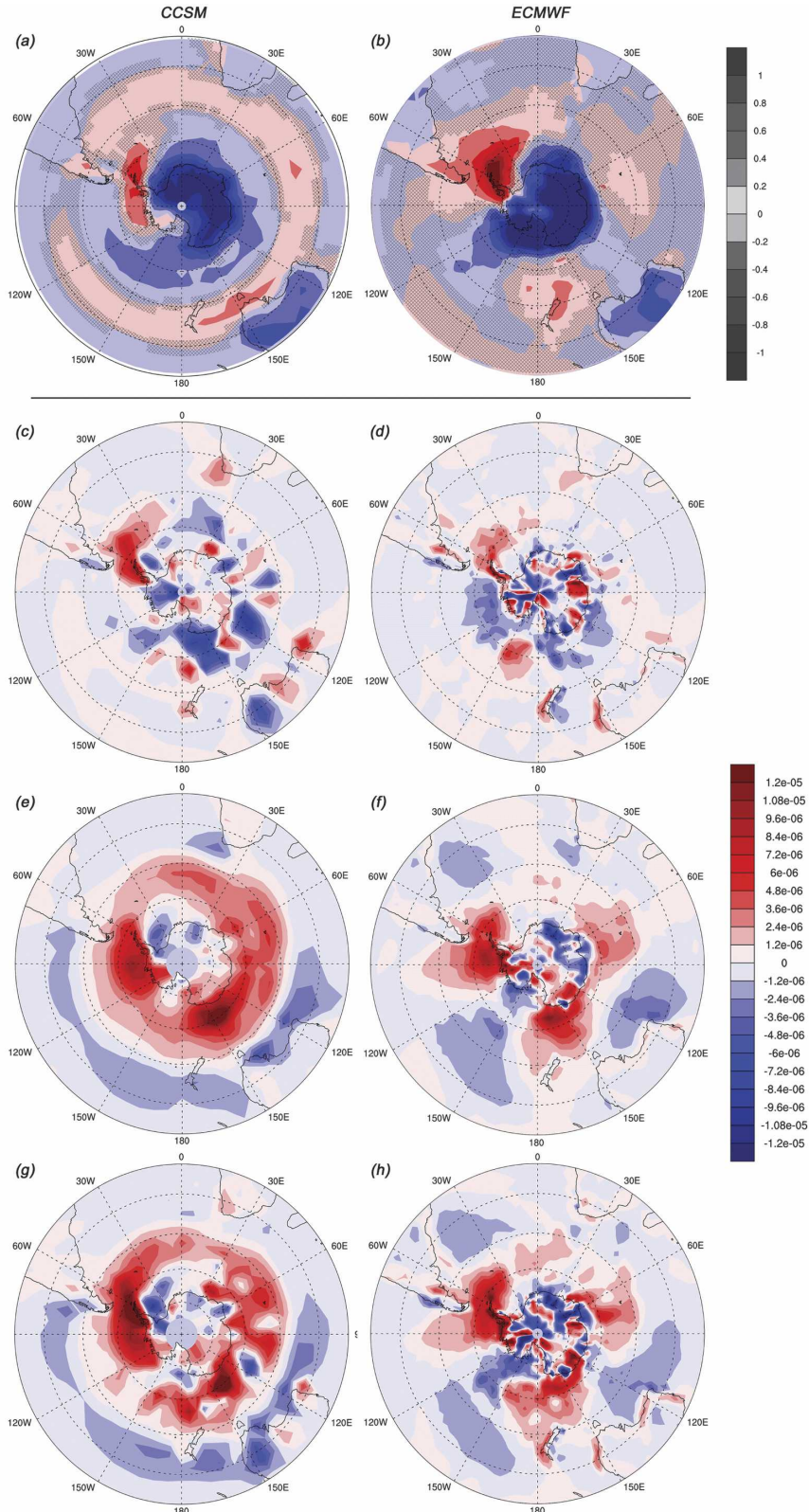


FIG. 5. Regression on the SAM index of (a) CCSM and (b) ECMWF surface temperatures (K). (c), (e), (g) CCSM and (d), (f), (h) ECMWF (c), (d) zonal, (e), (f) meridional, and (g), (h) zonal + meridional heat advection terms regressed on the SAM index ( $\text{K s}^{-1}$ ). Cross hatching indicates areas where confidence levels are below 95% (90%) for simulation (observation). Confidence levels are calculated using the method described by Sciremammano (1979).

served, with significant warming extending northward to southern South America and eastward to the Greenwich meridian. Also, the simulated area of warming around Tasmania is shifted eastward and sits over the South Island of New Zealand in the observations. Over the Antarctic continent, Thompson and Wallace (2000) describe an equivalent pattern in station air temperature data and postulate that the anomalous warming over the Antarctic Peninsula is a result of enhanced zonal advection of relatively warm oceanic air. Lefebvre et al. (2004) additionally suggest that nonzonal departures from the annular mode, which result in the more poleward wind anomalies described earlier, advect heat southward across strong meridional temperature gradients. A further interesting feature common to both model and observations is that over much of continental Australia a modest cooling occurs. These features are statistically significant at the 95% confidence level, and the fact that they occur in both simulation and observations suggests that they are robust.

To provide a more quantitative analysis of the importance of the zonal and meridional atmospheric advection of heat, we regressed the lateral surface heat budget terms

$$\left( -u \frac{\partial T^S}{\partial x} \right)', \quad \left( -v \frac{\partial T^S}{\partial y} \right)'$$

onto the SAM index, where  $(u, v)$  are the zonal and meridional surface wind velocities,  $T^S$  is the surface air temperature, and prime denotes anomalies from the long-term climatological monthly mean. The regression of these heat advection terms is shown in Fig. 5 for both model and observations. Both components cause a warming of the Antarctic Peninsula region; the zonal contribution is due to the larger mean zonal temperature gradient that exists in the region (figure not shown) and the meridional component is due to the relatively large meridional wind anomalies associated with deviations in the zonally symmetric pressure field (Fig. 2). The simulation shows a cooling over southeastern Australia due to zonal advection. However this region is more confined than the temperature response seen in Fig. 5, and the observations do not show a similar cooling effect. Regressions of other atmospheric heat budget terms (not shown) suggest that, for the CCSM, convective adjustment processes are driving the negative/positive anomalies over the Australian mainland/Tasmania.

Investigation of the lagged response to the SAM shows that the midlatitude SAT anomalies seen in Fig. 5 remain significant for many months, well beyond the period that advective atmospheric heat transport per-

sists. This suggests the possibility of a positive heat feedback from the oceans. This issue is discussed in the next section.

Significant changes in atmospheric moisture, total cloud cover, and total precipitation (Fig. 6) are also associated with the SAM. The precipitation response, in particular, shows good correspondence between observation and simulation (Figs. 6c,d), with potentially important consequences for regions with altered rainfall over land. For example, a positive phase of SAM is linked to decreased rainfall over southern Chile, southern New Zealand, and Tasmania and increased rainfall over eastern Australia and southern South Africa.

### b. Ocean

The SAM wind anomalies have both a dynamic (e.g., via Ekman transport) and thermodynamic effect on the ocean through surface stresses and by affecting heat and freshwater fluxes, respectively. A comparison between the SAM regression onto the simulated and observed horizontal surface currents [the latter from the Simple Ocean Data Assimilation (SODA) reanalysis dataset] is shown in Fig. 7. The observed flow anomalies have the same zonally symmetric structure and are of slightly reduced magnitude compared to the simulation, consistent with the weaker observed winds. The simulated flow shows maximum positive anomalies between  $50^\circ$  and  $60^\circ\text{S}$  and weaker minimum negative anomalies between  $30^\circ$  and  $40^\circ\text{S}$ . The reanalysis fields are more contracted toward the Pole with a maximum positive anomaly closer to  $60^\circ\text{S}$ . This is most likely linked to similar differences in the simulated and observed mean-state currents and ultimately with differences in the overlaying mean-state wind field (Fig. 3a). As with the atmospheric properties, both simulated and observed SAM responses result in a poleward contraction of the centers of maximum zonal and meridional flow, with anomalous responses approximately an order of magnitude smaller than the mean-state values. The meridional ocean response to the SAM is most likely due to surface Ekman transport anomalies (forced by the zonal wind fields of Fig. 2). The zonal ocean current response may be due to geostrophic and/or Ekman transport effects (as described below). The zonal and meridional CCSM responses are in good agreement with the corresponding EOFs (Fig. 1), which each explain  $\sim 15\%$  of the total surface circulation variability. The largest discrepancies between the simulation and the observed reanalysis occur in the Bellingshausen Sea and Drake Passage areas. Here, the more poleward observed wind response drives a stronger zonal component and a weaker meridional component to the oceanic Ekman transport.

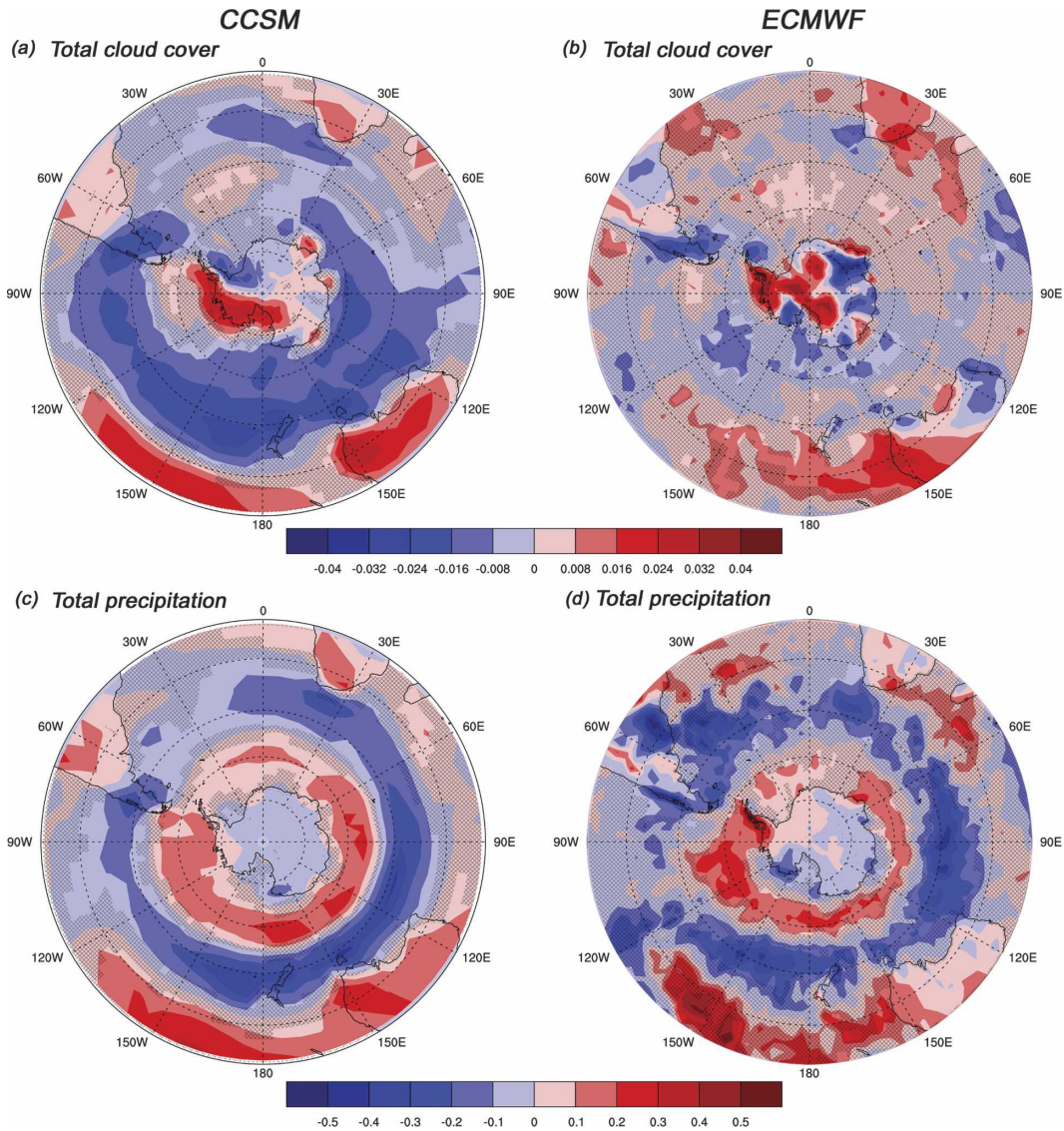


FIG. 6. (a), (b) Regressed total cloud cover (%) and (c), (d) total precipitation ( $\text{mm day}^{-1}$ ) for (a), (c) CCSM and (b), (d) ECMWF. Cross hatching indicates areas where confidence levels are below 95% (90%) for simulation (observation).

The modeled response of the horizontal ocean circulation to the SAM is primarily restricted to the surface layers (Fig. 8) with both meridional and zonal flow being significantly correlated to the SAM index (with maximum correlation at 0-lag). This suggests that any acceleration of the surface flow is largely a result of an enhanced Ekman transport or altered density structure near the surface. As the wind stress anomalies due to the SAM generally have a meridional as well as a zonal component, some of the zonal flow response will be directly wind driven. In addition, the redistribution of temperature and salinity acts to alter isopycnal gradients, particularly in the surface layers (Fig. 9a), through

which the thermal wind balance leads to an acceleration of the zonal flow at  $\sim 40^{\circ}\text{--}60^{\circ}\text{S}$  and a deceleration at  $\sim 20^{\circ}\text{--}40^{\circ}\text{S}$  during the positive phase of the SAM (Fig. 9b). However, since the density structure is only significantly altered in the surface levels, the anomalous flow (calculated as the depth integral of

$$-\frac{g}{\rho_0 f} \frac{\partial p}{\partial y}$$

from a depth of no motion of  $\sim 1000$  m) is an order of magnitude smaller than that associated with the anomalous Ekman transport. In addition, the lagged correla-

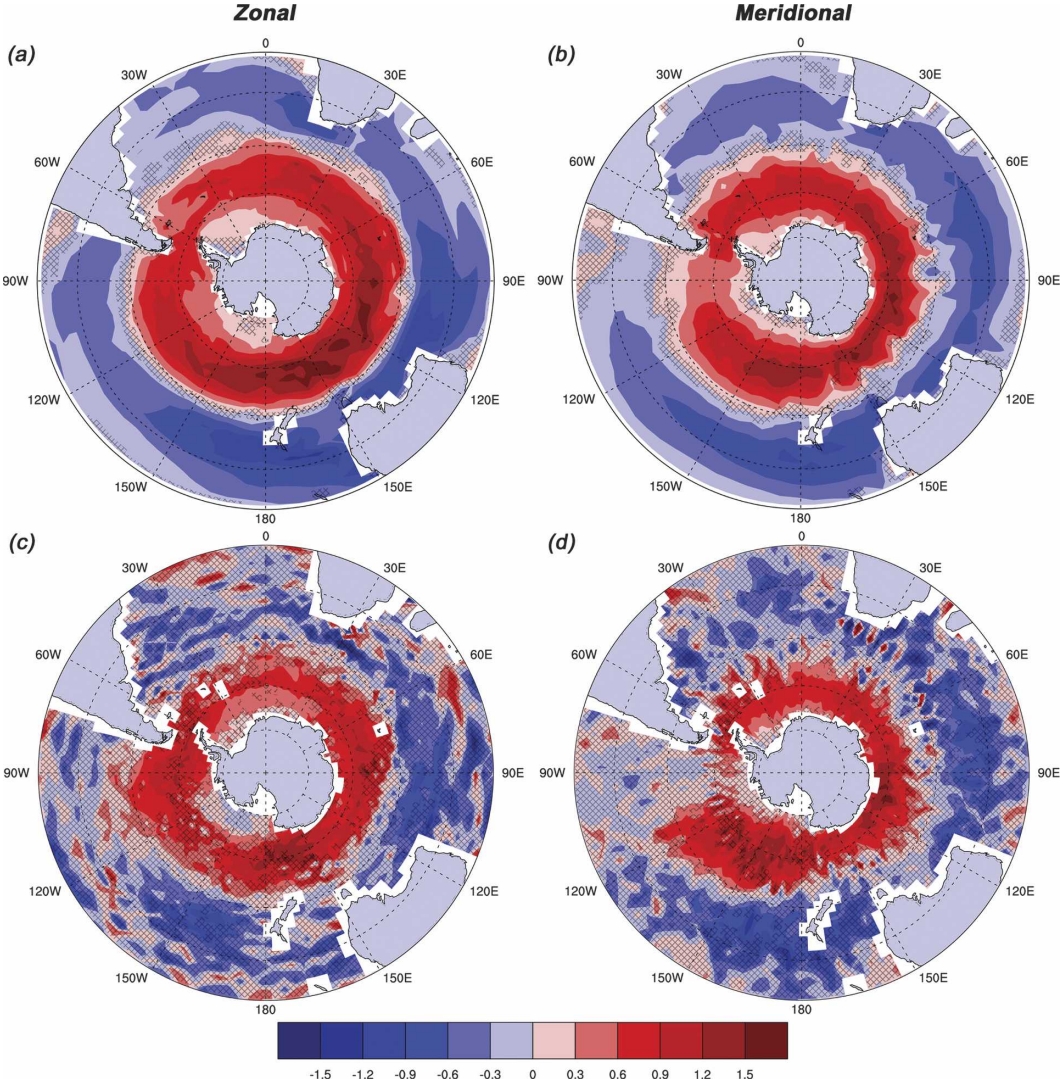


FIG. 7. (a), (c) Zonal and (b), (d) meridional surface current anomalies ( $\text{cm s}^{-1}$ ) regressed onto the SAM index for the (a), (b) model and the (c), (d) SODA reanalysis. The SODA data have been subsampled to remove high-frequency noise resulting from sparse data assimilation. Cross hatching indicates areas where confidence levels are below 95% (90%) for simulation (observation).

tion of the zonal flow shows the response decaying quickly, consistent with a wind-driven flow, unlike a density-driven flow where temperature and salinity anomalies persist much longer. The final conclusive indication that the surface current response is predominantly wind driven is that the vertical structure of the regressed horizontal flow (not shown) has an increasing angle relative to the wind vector together with a diminishing magnitude with increasing depth, indicative of an Ekman spiral. Such a profile would not be compatible with a primarily density-driven flow. Hall and Visbeck (2002) show that their modeled surface current response closely matches a derived Ekman flow calculated from the surface wind stress response, although

small discrepancies do exist. This is consistent with our results that reveal only a minor additional component due to a thermal wind adjustment to the SAM.

Although much smaller than the surface current, a zonal barotropic component of flow is evident to great depth (Fig. 8c). This is driven by the anomalous sea surface slope set up by the SAM-induced meridional Ekman transport. As with the surface currents, the barotropic flow responds almost instantaneously to the surface winds. While the magnitude of the barotropic response is significantly smaller than the surface flow response, its extent is great and, as a result, the SAM-induced zonal transport for the ocean interior is significantly greater than for the surface layers alone. Hughes

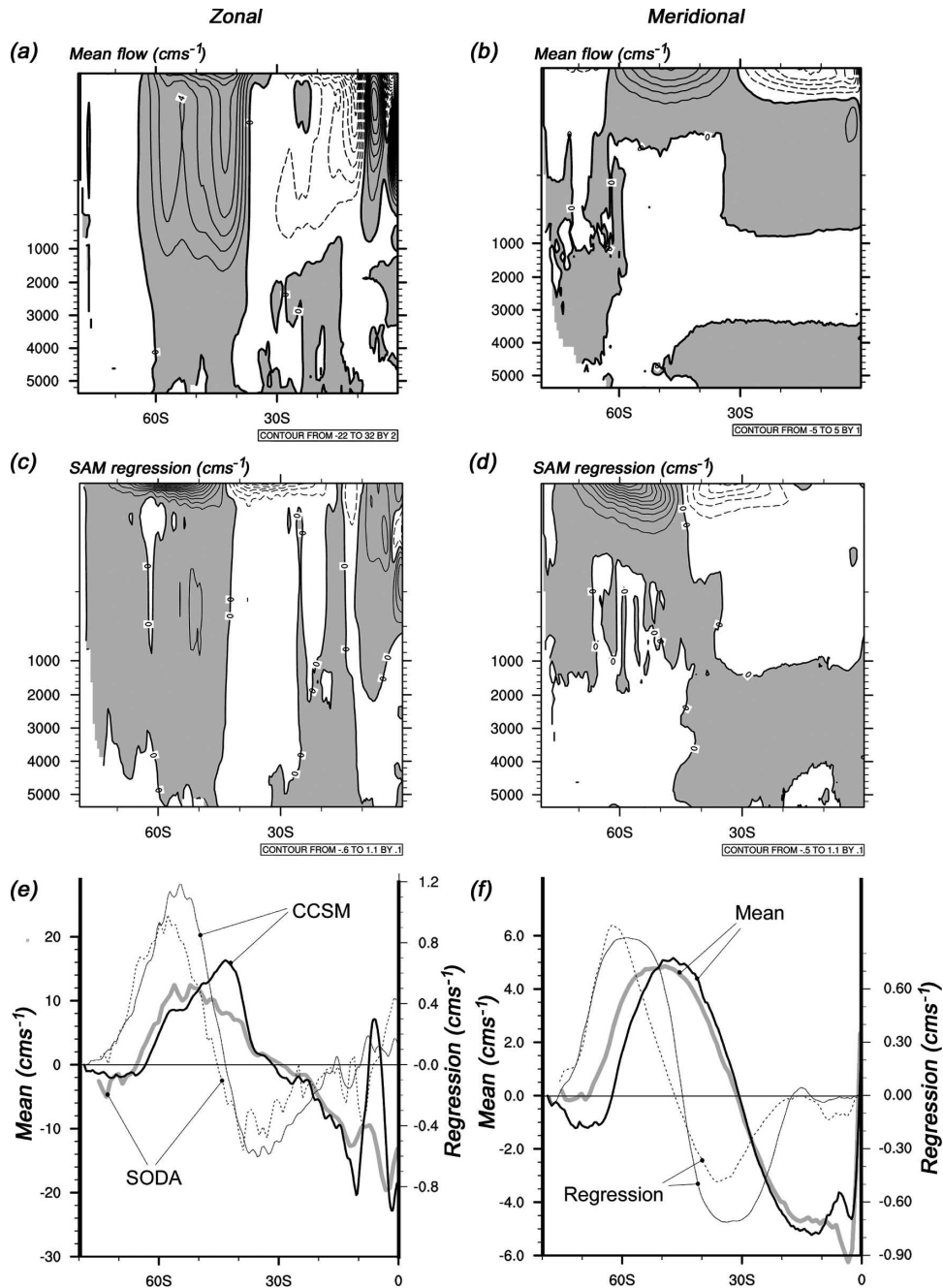


FIG. 8. Zonally averaged (a), (c), (e) zonal and (b), (d), (f) meridional ocean currents. The (a), (b) annual mean currents, (c), (d) SAM-regressed currents, and (e), (f) annually averaged CCSM (thick black contour, left-hand scale), annual-averaged SODA reanalysis (thick gray contour, left-hand scale), regressed CCSM (thin contour, right-hand scale), and regressed SODA reanalysis (dotted contour, left-hand scale) currents. All values are given in units of  $\text{cm s}^{-1}$ .

et al. (2003) and Meredith et al. (2004) find high observed correlations between the variability of transport through Drake Passage and the SAM. Using transports derived from a realistically forced high-resolution OGCM (OCCAM) in conjunction with subsurface

pressure measurements, Hughes et al. (2003) finds a transport increase of 3.5 Sv ( $\text{Sv} \equiv 10^6 \text{ m}^3 \text{s}^{-1}$ ) for a one standard deviation positive SAM index (based on a relatively short 10-yr record). This compares well with the CCSM Drake Passage transport anomaly of  $\sim 4$  Sv

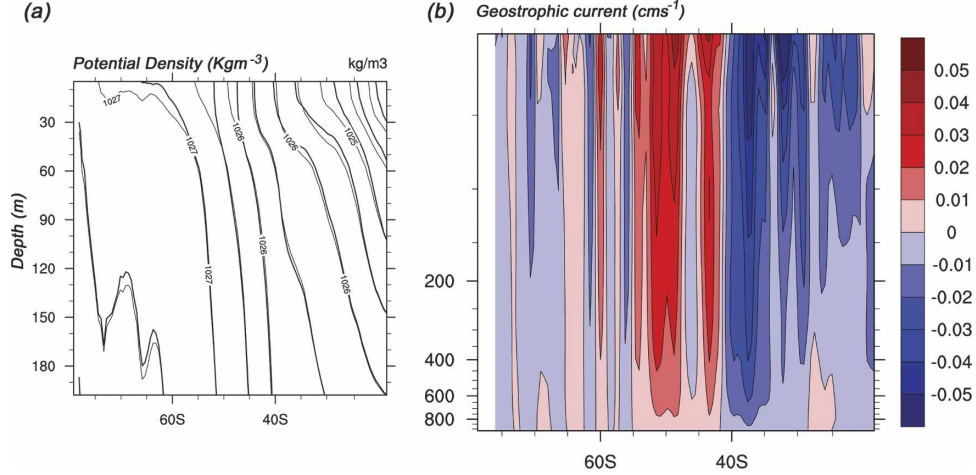


FIG. 9. (a) Potential density ( $\text{kg m}^{-3}$ ) composites of positive (thick lines) and negative (thin lines) SAM calculated for values  $>|2 \text{ standard deviation}|$  of the SAM index. (b) The regressed geostrophic current ( $\text{cm s}^{-1}$ ) due to SAM. Note that (a) and (b) have different depth axis scales.

for a one standard deviation SAM (with a correlation of 0.56 between the SAM index and Drake Passage transport time series). In the coarse-resolution coupled model of Hall and Visbeck (2002) a much weaker response is observed; they find only an  $\sim 0.63 \text{ Sv}$  SAM transport (correlation 0.49). This is likely due to their model's coarse resolution and their Drake Passage transport exhibiting a significantly weaker mean transport (76.1 Sv) compared to the CCSM (122 Sv). The latter is much closer to the observed value of  $\sim 130 \text{ Sv}$ .

The convergent meridional flow anomaly causes enhanced downwelling centered near  $45^\circ\text{S}$  straddled by two overturning cells (with maximum variance at 0-lag) centered between  $30^\circ$  and  $40^\circ\text{S}$  to the north and at  $\sim 55^\circ\text{S}$  to the south (Fig. 10). Both cells reach to sig-

nificant depths, between 3000 and 4000 m, and are strongly correlated with the SAM index. The cells act to reinforce, and shift southward, the wind-driven "Deacon" overturning cell, substantially enhancing the simulated transport by  $\sim 6 \text{ Sv}$  from an annual-mean value of  $\sim 14 \text{ Sv}$  at a depth of 3000 m. This has the potential to alter the production and properties of Subantarctic Mode and Antarctic Intermediate Waters that form near this latitude band. The deep response of the ocean's meridional overturning circulation is a robust feature that is evident in other ocean simulations (e.g., Hall and Visbeck 2002; Lefebvre et al. 2004; Cai and Watterson 2002). Using the Commonwealth Scientific and Industrial Research Organisation (CSIRO) Mk2 coupled climate model Cai and Watterson (2002) dem-

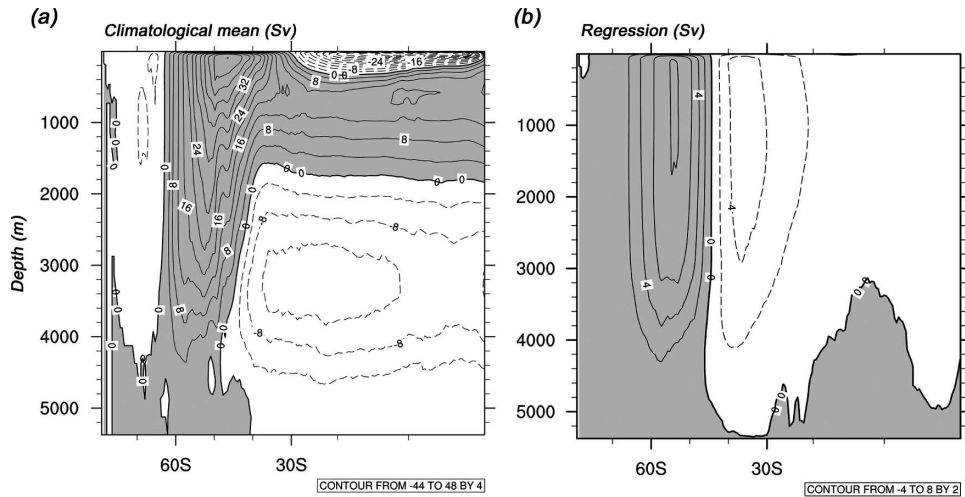


FIG. 10. Zonally averaged (a) annual mean and (b) regressed meridional overturning streamfunction. Values are given in Sv.

onstrate that the dominant EOF of meridional overturning (explaining 51% of variance) is closely linked to the SAM. Furthermore, Oke and England (2004) find an increase in the formation of AAIW associated with a poleward shift in the subpolar westerlies in a coarse-resolution OGCM. This is associated with a cooling and freshening of intermediate waters in their simulation.

To investigate the SAM effect on intermediate water pathways, we form a linear interpolation of the horizontal flow fields along the  $\sigma_{27.2}$  isopycnal and regress it onto the SAM index. The  $\sigma_{27.2}$  isopycnal closely follows the salinity minimum that traditionally identifies the pathway of intermediate water into the interior and northward (Santoso and England 2004). As the southern outcrop of this isopycnal varies considerably with season, the analysis is restricted to four wintertime months, namely June–September (JJAS), over which the movement of the outcrop is relatively small and during which time most intermediate water is formed. Figure 11a shows the mean-state along-isopycnal JJAS flow field with the SAM response flow field (at 0-lag) superimposed. The mean flow shows a strong eastward circulation at  $\sim 40^{\circ}\text{--}50^{\circ}\text{S}$  following the Antarctic Circumpolar Current (ACC). Northward transport of intermediate water generally occurs at the eastern side of the basins followed by a recirculation as part of the subtropical gyres. The flow pathways closely follow lines of constant isopycnal depth, indicating the strongly geostrophic nature of the circulation. The simulated mean-state circulation is very similar to flow on the  $\sigma_{27.2}$  isopycnal in the CSIRO Mk2 coupled climate model and is also consistent with observed pathways (Santoso and England 2004, and references therein). The anomalous flow field is more complicated, particularly in the vicinity of the ACC, with many small-scale recirculations. Along  $\sigma_{27.2}$ , the zonal component of the anomalous flow tends to be eastward to the south of  $\sim 40^{\circ}\text{S}$  and westward to the north (Fig. 11b), in line with the enhanced wind-driven surface zonal current. The response components closely match the corresponding dominant EOFs of zonal and meridional velocity anomalies on  $\sigma_{27.2}$  (not shown), explaining 18% and 13% of variance, respectively. The meridional flow acts to enhance the mean northward transport at  $\sim 60^{\circ}\text{S}$ . On a regional scale there appears to be both coherent large-scale strengthening and weakening of various flow pathways. For example, northwestward flow to the south and west of Australia and South Africa is enhanced while the equivalent flow pathway in the Pacific is weakened (see yellow shaded regions of Fig. 11a).

Simulated SAM changes to both temperature ( $T$ ) and salinity ( $S$ ) are only of significant magnitude in the

upper ocean with maximum anomalies at the surface. These changes can occur through the advection (or mixing) of heat and freshwater across  $T\text{--}S$  gradients and/or via air-sea heat/freshwater fluxes. The regression of salinity onto the SAM (not shown) is relatively weak (although correlations are statistically significant; see Fig. 16), whereas the temperature response is highly significant with variations exceeding  $\pm 0.3^{\circ}\text{C}$  for a one standard deviation change in the SAM (Fig. 12). The simulated SST pattern has strong zonal symmetry with a band of cooler temperatures centered between  $50^{\circ}$  and  $60^{\circ}\text{S}$  and warmer temperatures at  $30^{\circ}\text{--}45^{\circ}\text{S}$ . This pattern matches closely the dominant SST EOF mode, explaining  $\sim 18\%$  of total SST variability (Fig. 1c). The thermal inertia of the ocean means that the temperature and salinity response is most highly correlated to the SAM at a lag of 1 month, although a significant response persists many months after the primary atmospheric SAM signal (described later; see Fig. 16). The SAM also projects weakly onto the strength of the polar fronts. Comparison of meridional SST gradient composites for extreme SAM states (not shown) shows that for positive events an intensification of the maximum gradient (indicative of the Subantarctic Front) occurs where the front is located at midlatitudes, while it weakens where the front is farther to the south (in the eastern Pacific). This is consistent with the response of meridional velocities to the SAM, which sees an increased convergence of waters near  $\sim 45^{\circ}\text{S}$ .

While both simulated and observed atmospheric and ocean surface current responses to the SAM are in close agreement, SST shows a poorer match, with the simulated response considerably stronger and more symmetric than the observed (Fig. 12b). The coarse-resolution model of Hall and Visbeck (2002) shows even greater zonal symmetry in SST than the CCSM—a result of their highly symmetric surface wind response. The observed response is much less zonally symmetric than that exhibited by the model, in particular due to a relatively cold anomaly between  $100^{\circ}$  and  $150^{\circ}\text{W}$  that extends to  $\sim 40^{\circ}\text{N}$ , in contrast to the warming at these latitudes in the model. This area corresponds to a region of enhanced equatorward transport that breaks the meridional current symmetry in the SODA reanalysis (Fig. 7). It is also coincident with a region of anomalously cold SAT that is more pronounced (relative to its surroundings) in the observed compared to the simulation (Fig. 5). Other discrepancies are also generally consistent with the differences in overlying SAT. It should be noted, however, that the reanalysis data spans only three decades and in situ coverage of SST is very sparse in the mid and high latitudes of the Southern Ocean, with different SST products showing large

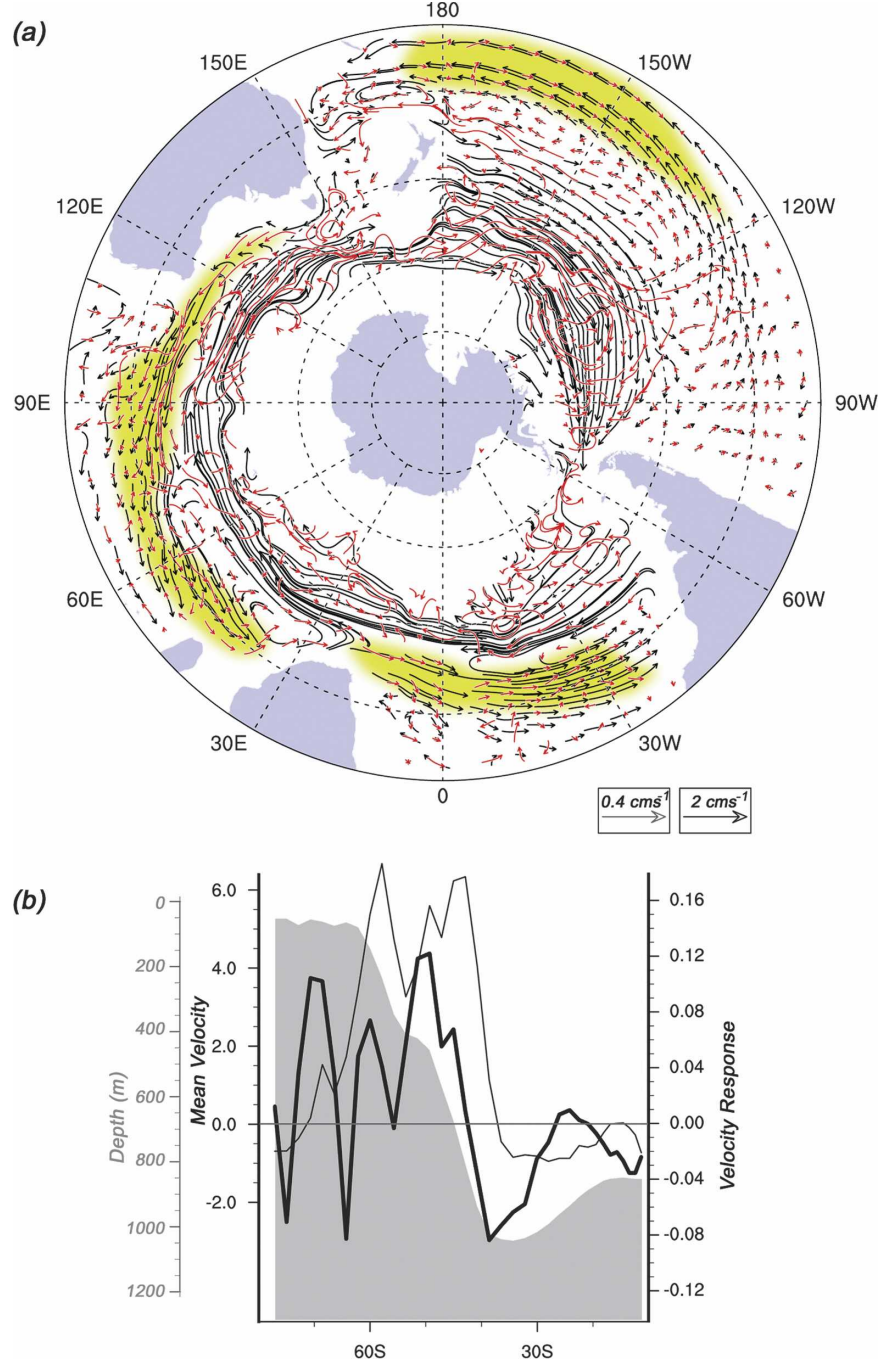


FIG. 11. (a) Lateral velocity on the  $\sigma = 27.2 \text{ kg m}^{-3}$  isopycnal for long-term annual mean (black) and SAM-regressed (red) velocity vectors. The two velocity fields are on different scales to emphasize anomalous flow due to the SAM; yellow shading indicates regions of coherent anomalies (see text). (b) Simulated zonally averaged mean (thick line, left-hand scale) and regressed (thin line, right-hand scale) zonal velocities ( $\text{cm s}^{-1}$ ). Gray shading and leftmost scale show the depth of the  $\sigma_{27.2}$  isopycnal surface (m) in the model.

time- and space-scale monthly rms discrepancies that exceed  $0.5^\circ\text{C}$  in some regions (Reynolds et al. 2002). As a result, the reanalysis results do not necessarily constitute an unambiguously accurate representation of the

real ocean's variability. The fact that the SST response is greatest at a lag of 1 month to the SAM demonstrates that it is atmosphere to ocean heat fluxes (not the other way around) that are forcing the temperature changes

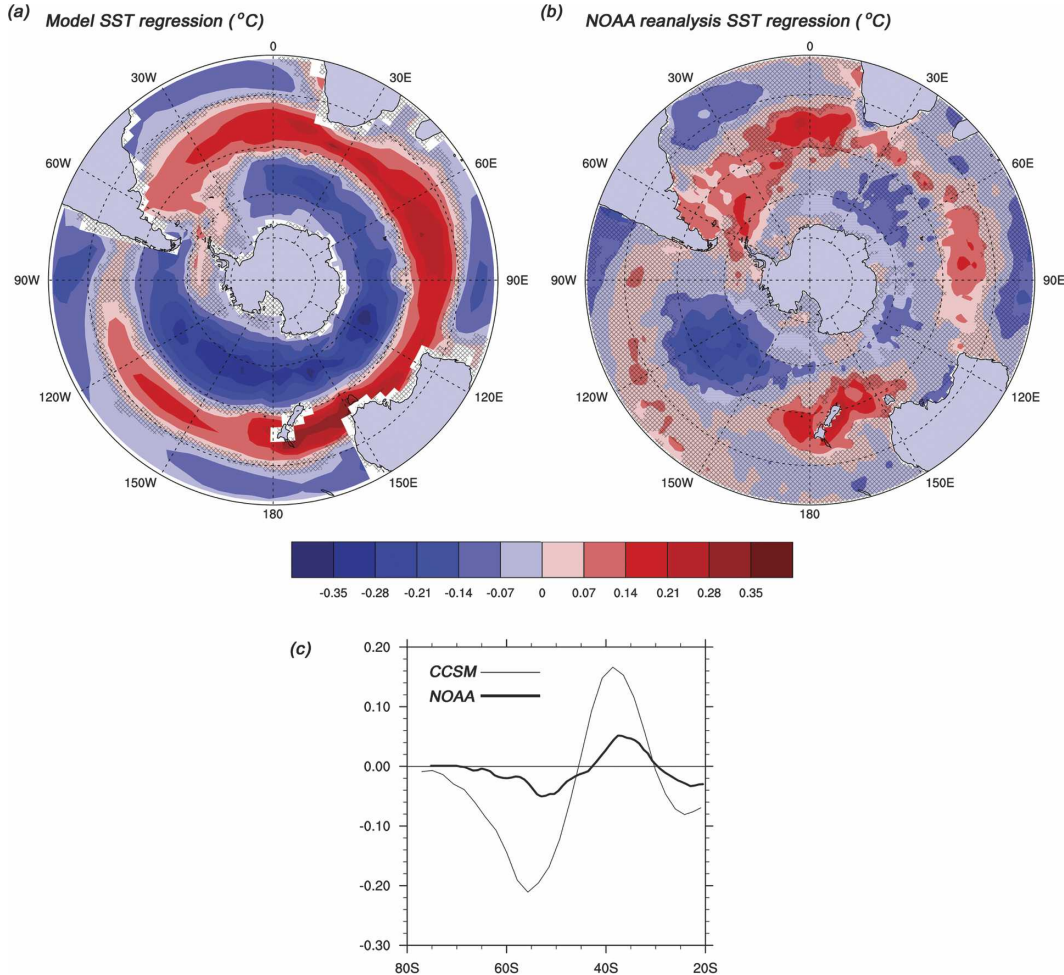


FIG. 12. Regression of (a) CCSM and (b) NOAA reanalysis SST on the SAM index. (c) Zonally averaged regression of SST on the SAM index (CCSM—thin line; NOAA—thick line). Values are given in °C. Regressions are shown as 1-month lagged values. Cross hatching indicates areas where confidence levels are below 95% (90%) for simulation (observation).

together with ocean advection responses during the buildup of the SST response.

To further investigate the mechanisms behind the changes in ocean temperature due to the SAM, we consider the heat budget in the ocean mixed layer. This relates the mixed layer temperature ( $T^M$ ) tendency to changes in mixed layer heat content via the net surface heat flux ( $Q_N$ ), zonal, meridional, and vertical advection of heat and mixing:

$$\frac{\partial T^M}{\partial t} = \frac{Q_N}{\rho_0 C_p(\text{MLD})} - u \frac{\partial T^M}{\partial x} - v \frac{\partial T^M}{\partial y} - w \frac{\partial T}{\partial z} \Big|_{\text{MLD}} + \text{mixing}$$

where  $\rho_0$  is density,  $C_p$  is the specific heat of seawater,  $(u, v)$  are the eastward and northward components of ocean velocity averaged over the mixed layer, and

MLD represents the monthly mixed layer depth. The vertical advection term ( $w$ ) is evaluated at the base of the mixed layer. By virtue of averaging over the mixed layer, most convective (and diapycnal) mixing is implicit in the analysis. In addition, the isopycnal and eddy mixing terms tend to damp out, rather than enhance, anomalies; we do not attempt to further evaluate these terms (see also Rintoul and England 2002). An examination of model versus observed temperature stratification in the Southern Ocean (not shown) reveals that the CCSM simulation of  $dT/dz$  is of the correct order of magnitude at the base of the surface mixed layer. In addition, Ekman pumping velocities are the major contributor to ( $w$ ) at the base of the surface mixed layer, and these are well resolved as they depend on horizontal wind stress gradients. Thus, model values of  $wdT/dz$  variability are likely to be close to the observed. Re-

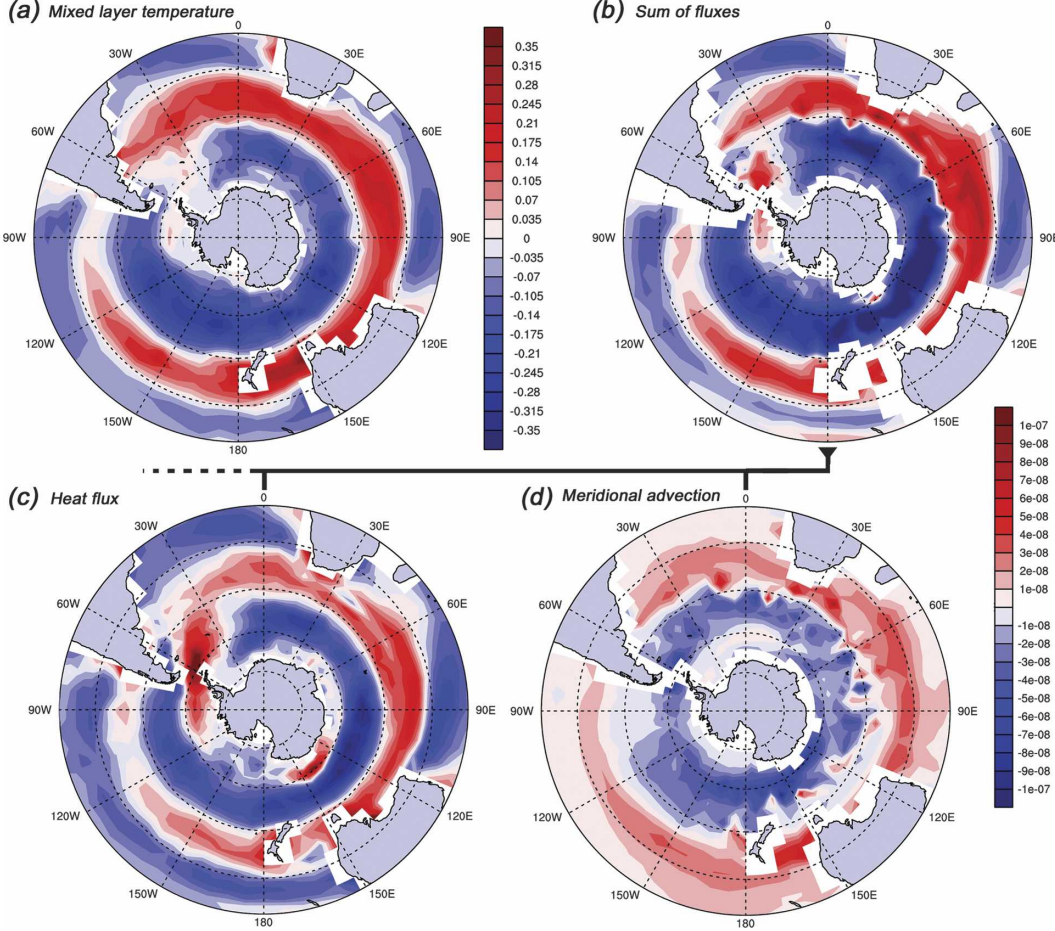


FIG. 13. Regressions on the SAM index of (a) mixed layer temperature ( $^{\circ}\text{C}$ ), (b) sum of mixed layer heat budget terms ( $\text{^{\circ}\text{C s}^{-1}}$ ), (c) net surface heat flux term ( $\text{^{\circ}\text{C s}^{-1}}$ ), and (d) meridional heat advection term ( $\text{^{\circ}\text{C s}^{-1}}$ ). Color scaling is identical in (b)–(d).

gressions of the main heat budget terms are shown in Fig. 13. In general, the sum of forcing terms is in good qualitative agreement with the mixed layer temperature regression (Figs. 13a,b), suggesting a closed heat budget in this analysis. The budget is dominated by the net surface heat flux term (Fig. 13c) and, to a lesser extent, the meridional advective transport term (Fig. 13d). The other terms (not shown) make much smaller contributions. In their investigation of the oceanic response to the SAM, Lefebvre et al. (2004) suggest that upwelling can play an important role in SST changes. Here we find little evidence for this, with the effect of vertical advection an order of magnitude smaller than the meridional advection. Both dominant terms, air-sea heat flux and meridional advection, have strong zonal symmetry with complementary cooling south of  $45^{\circ}\text{S}$  and heating northward to  $\sim 30^{\circ}\text{S}$ . The fact that the two dominant terms show a response to the SAM of roughly equal sign south of  $30^{\circ}\text{S}$  means that the annular mode

has a substantial effect on ocean heat content. North of  $30^{\circ}\text{S}$  the two terms have opposing effects and result in a weak net cooling in the mixed layer. A substantial departure from zonal symmetry occurs in the localized region of DP where  $Q_N$  shows a heating response. This heating is opposed by the cooling from the meridional advection, resulting in an area of weak SAM-related SST response.

The surface heat flux may be further broken down into constituent terms, such that

$$Q_N = Q_R + Q_S + Q_L + Q_M,$$

where  $Q_R$  is the net radiation (net longwave + net shortwave),  $Q_S$  is the sensible heat flux,  $Q_L$  is the latent heat flux, and  $Q_M$  is the heat flux due to melting ice (Fig. 14). There is a large area at midlatitudes extending from the Drake Passage eastward to the south of Australia where all three components of the net air-sea heat flux conspire to produce an anomalous ocean heat

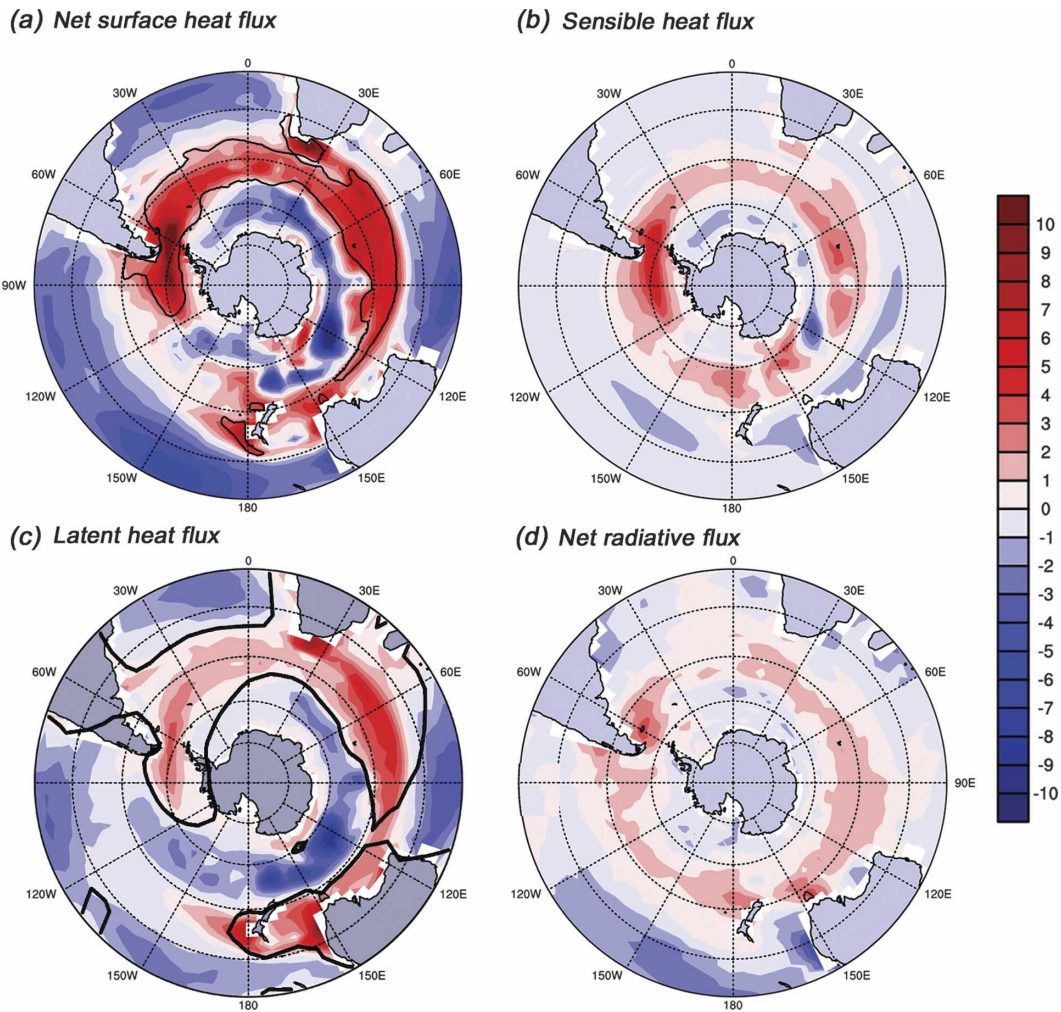


FIG. 14. Regression of simulated surface (a) net, (b) sensible, (c) latent, and (d) net radiative heat fluxes ( $\text{W m}^{-2}$ ) on the SAM index. The superimposed contour on the net heat flux in (a) shows the region where all component forcings coincide to produce a positive flux. Superimposed on the latent heat flux in (c) is the zero contour of regressed specific humidity.

gain during the positive phase of the SAM (Fig. 14a). Overall, the net atmosphere–ocean heat flux regression is dominated by latent and sensible heat fluxes, with a weaker contribution from the net radiation (Fig. 14). Sensible and latent heat fluxes are both proportional to the wind speed above the ocean and to the surface temperature and water vapor content gradients, respectively. Sensible and, to a lesser extent, latent heat fluxes are enhanced in the DP area. This results from the enhanced SAT (Fig. 5) and surface moisture content in this region initially exceeding the corresponding sea surface response. In general, the pattern of surface latent heat flux is broadly consistent with the surface specific humidity response with negative values between  $45^{\circ}$  and  $60^{\circ}\text{S}$  away from DP and with positive anomalies farther north except in the central and western Pacific.

This is highlighted by the superimposed zero contour of specific humidity regression on the latent heat diagram (Fig. 14c). The particularly strong negative response between  $\sim 110^{\circ}$  and  $170^{\circ}\text{E}$  results from the enhanced surface wind speed response, which is greatest in this region. Away from the DP region, the surface sensible heat flux response is somewhat weaker and clearly not determined by the SAT pattern alone. A comparison of the relative SST and SAT responses shows that the cooling of the ocean between  $45^{\circ}$  and  $60^{\circ}\text{S}$  is larger than the cooling of the air above in much of the circumpolar band away from the DP region, resulting in the positive sensible heat flux response at these latitudes. Again, the enhanced wind in this band tends to magnify the regression fluxes.

The patterns of regressed total surface heat flux (Fig.

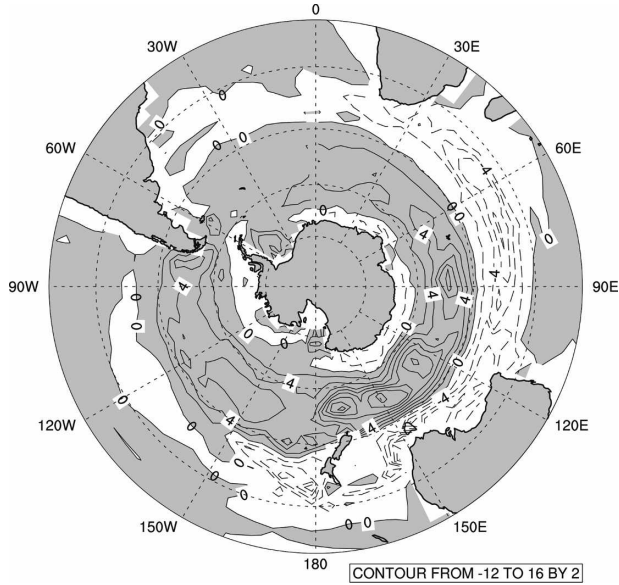


FIG. 15. Regression of monthly maximum mixed layer depth (m) on the SAM index. Positive values (shaded) indicate mixed layer deepening.

14a) and the regressed heat flux term of the mixed layer budget exhibit some subtle differences (Fig. 13c). This results from the mixed layer depth response to the SAM (Fig. 15), which scales the air-sea heat flux terms in the mixed layer budget. Mixed layers show a general deepening between 45° and 60°S and shoaling between 30° and 45°S. Deepening (shoaling) will result in a reduced (increased) mixed layer response to the surface heat flux terms. This produces the more zonally symmetric form of the net surface heat flux term except in the DP region where the mixed layer response is weak. The mixed layer depth anomalies (Fig. 15) are consistent with both the pattern of the wind speed response (where stronger winds will tend to deepen the mixed layer) and with a feedback effect on ocean temperatures (where cooler surface temperatures lead to conditions more favorable to density-driven convective overturning).

An interesting feature of the SAT response in this model is its strong persistence long after other atmospheric anomalies have decayed. Lagged correlations (Fig. 16) reveal that, although the advection-driven SAT changes over Antarctica decay quickly (in line with the rapid decay of the surface wind response), the SAT anomalies over the Southern Ocean are evident and are in close correspondence with SST for many months. Much of this coupling appears to be due to latent heat fluxes whose direction tends to reverse after the initial response period. At 0-lag rapid changes in atmospheric humidity drive the latent heat fluxes, while

at longer lags the more persistent anomalies in the high-inertia ocean drive the latent heat fluxes (with a corresponding change in polarity of the latent heat flux anomaly pattern; Fig. 16). This helps couple the SAT response to SST over these longer time scales. Here, at least, we see a significant feedback to the atmosphere via oceanic forcing. Although lagged correlation patterns for observed SAT and SST are less conclusive, the SAT responses do show equivalent statistically significant regions of long-term persistence in line with the SST anomalies (figure not shown). As outgoing long-wave radiation (OLR) is a function of not only cloud cover but also SST the simulated OLR response (Fig. 16) also persists for many months in tandem with the SST response.

### c. Sea ice

Drag forces associated with the SAM anomalous surface wind and ocean circulation, as well as the various thermodynamic forcings, also affect the advection and formation/melting of sea ice. As the pattern of sea ice is very different between summer and winter, to investigate the effect of the SAM on sea ice we select Southern Hemisphere summer [January–April (JFMA)] and winter (JJAS) subsets of the data corresponding to times of minimum and maximum ice coverage, respectively. Figure 17 shows the response of ice velocity and sea ice concentration to the SAM at 0-lag and at a lag of 1 month to the SAM, respectively, for JFMA and JJAS. The greatest velocity response is coincident with maximum surface wind and current responses (0-lag), while ice extent shows larger responses at higher lags. The SAM-induced change in ice coverage at the ice edge (shown by the 5% and 50% contours) is well explained at most locations by anomalous ice advection. At most longitudes and for both seasons, sea ice velocity has a strong eastward component in line with the SAM-related stresses exerted by the ocean and the wind. There is also significant northward transport over much of the domain consistent with the oceanic and ice Ekman transport response. The most prominent exception occurs primarily to the west of the Antarctic Peninsula ( $\sim 50^{\circ}$ – $120^{\circ}$ W) in JJAS, where there is an intensified southward component to the winds during the positive SAM phase and the corresponding meridional Ekman response is weak (Figs. 7b,d).

In the vicinity of DP and the South Atlantic there is a contraction in the ice edge across much of the region where the climatological ice boundary is aligned northeastward and an ice extension where the ice is aligned southeastward (see ice-edge contours, Fig. 17). This is particularly evident near the Greenwich meridian during the summer season and between  $30^{\circ}$  and  $120^{\circ}$ W

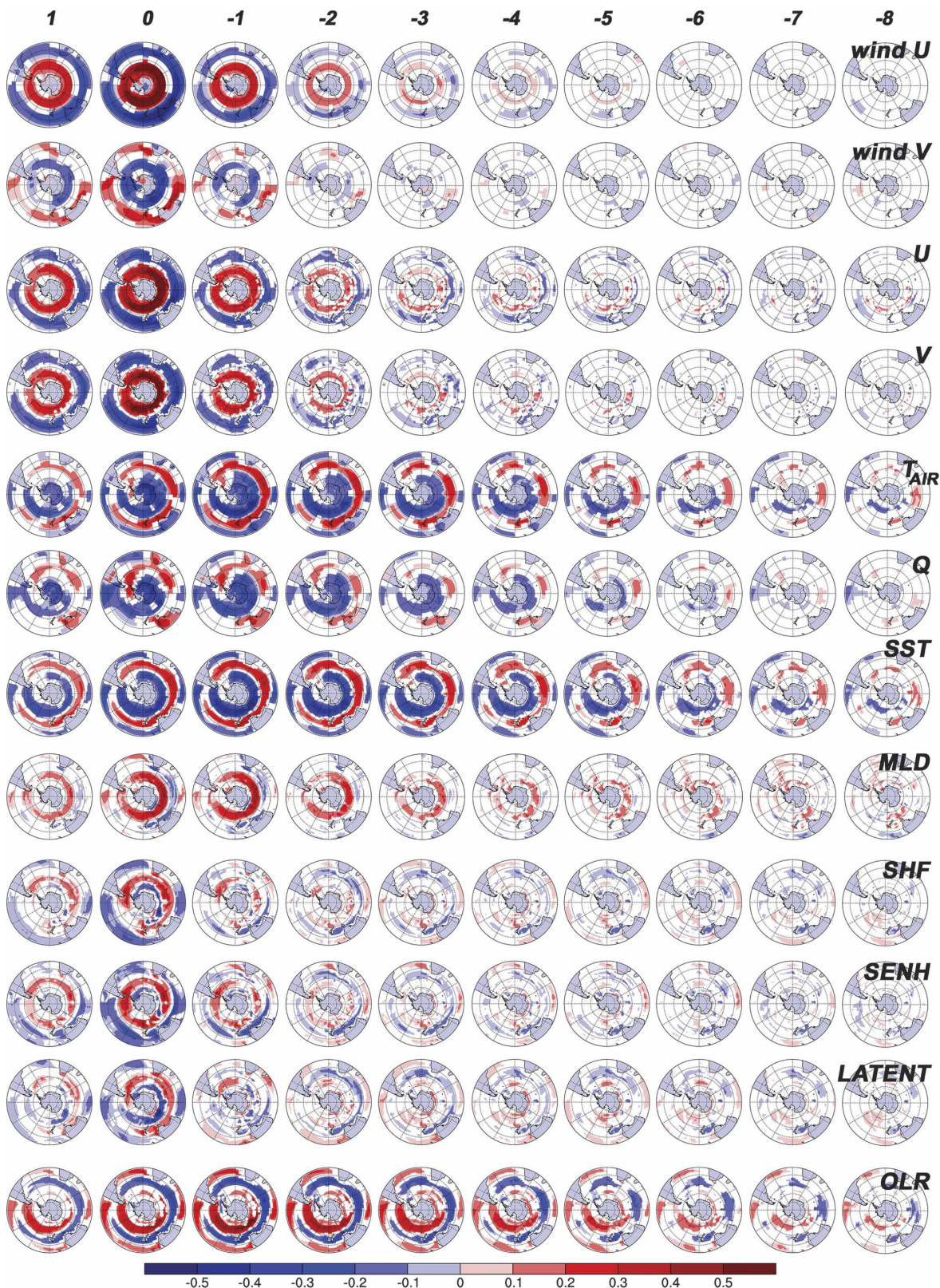


FIG. 16. CCSM correlation maps at multiple lags (1 to  $-8$  months; negative lags imply SAM leading). Only correlations with greater than 95% confidence are shown.

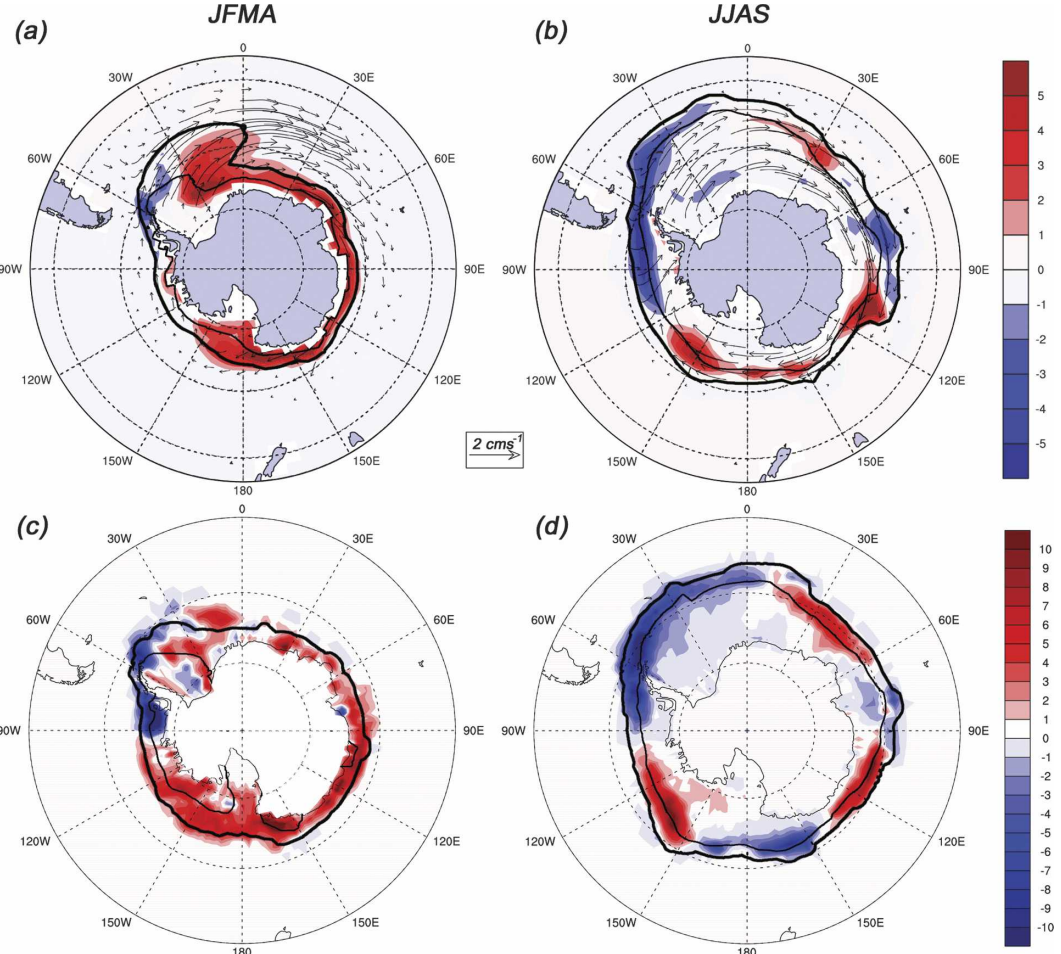


FIG. 17. (a), (b) CCSM and (c), (d) HadISST reanalysis regressions on the SAM index of sea ice concentration lagged by 1 month (color shading) for the (left) JFMA and (right) JJAS seasons. Ice concentration regression values are shown as percentage cover. CCSM plots also show sea ice anomaly velocity vectors ( $2 \text{ cm s}^{-1}$  vector scale is shown). Thick (thin) contour lines represent the seasonally averaged 5% (50%) ice coverage extent. NB: Velocity vectors north of the 5% contour are often in regions where contouring does not resolve response magnitudes.

during winter. The SAM-induced zonal advection also leads to a significant thinning of the ice (not shown) along the eastern flank of the Antarctic Peninsula with a corresponding thickening farther east. This mechanism (whereby predominantly zonal ice advection causes an effective meridional increase in ice cover), by virtue of the ice-edge orientation, is also evident at other locations, for example near  $180^\circ$  for JFMA and around  $30^\circ\text{E}$ ,  $75^\circ\text{E}$ ,  $110^\circ\text{E}$ , and  $150^\circ\text{W}$  for JJAS. Under this mechanism alone, one would expect the positive ice coverage anomaly east of  $\sim 30^\circ\text{W}$  to extend to at least  $40^\circ\text{W}$  during summer, which is not the case. The discrepancy is accounted for by the anomalous SAT warming in this region, which acts to melt the sea ice. This SAM-induced warming of SAT also amplifies the negative anomaly in the DP region apparent during

JJAS. Holland et al. (2005) present a similar analysis of ice cover response to the SAM in the CCSM. They find a maximum ice response to the SAM at a lag of 1 yr, which they attribute to an ice-albedo feedback mechanism. Our analysis finds no such year-delayed maximum response but instead a maximum variance at between 1- and 5-month lag to the SAM depending on location (Fig. 18). The lagged response does, however, show considerable persistence, with anomalies lasting into the subsequent year. The fact that the maximum response at various locations often occurs after the time of maximum external forcing (from both the atmosphere and ocean) suggests that an ice-albedo feedback process is, indeed, operating to facilitate the persistence of the ice response. An interesting imbalance between summer and winter seasonal responses can be seen,

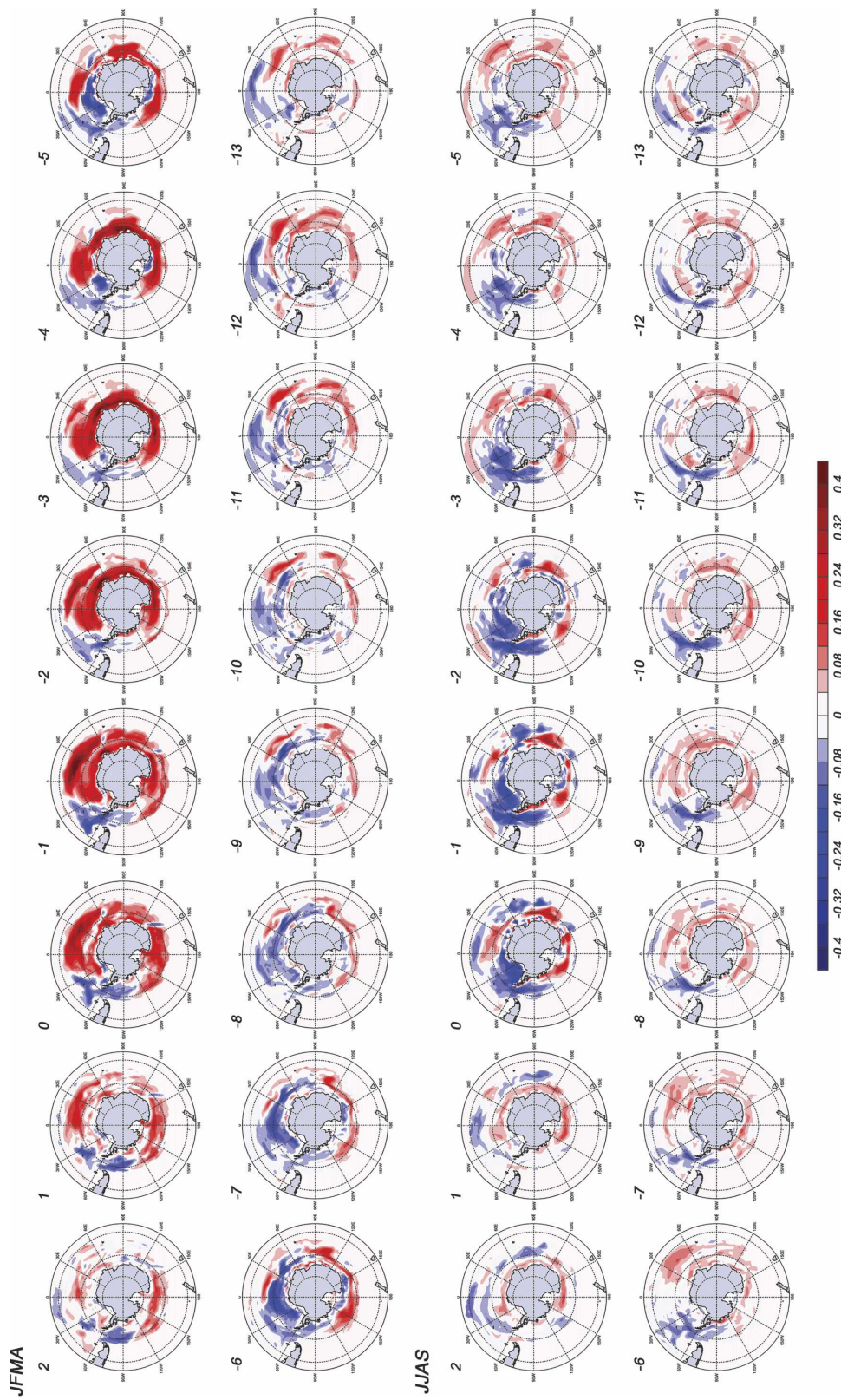


FIG. 18. CCSM sea ice concentration correlation maps at multiple lags (+2 to -13 months; negative lags imply that the SAM index leading ice coverage).

whereby a summer SAM event produces almost as large a response the following winter as a winter SAM event can produce at short lags. This results from the more pronounced ice-albedo feedback that occurs when high-latitude insolation is strong.

The pattern of simulated seasonal ice response is broadly consistent with observed data taken from the HadISST reanalysis, although the simulated response is weaker by about a factor of 2. Again, the short record length (only three decades of data that include some level of satellite assimilation) and sparsity of high southern latitude in situ measurements hamper the study of variability in the real system. During JFMA the circumpolar response is predominantly an increase in ice coverage except in the region near the Antarctic Peninsula. During JJAS the contraction in the South Atlantic is more pervasive than in the model, extending significantly farther eastward. There are two major areas of model–observed disagreement. The first occurs to the east of the Ross Sea region in both seasons, where the observed positive anomaly has a larger extent than the simulation. This area corresponds to the region with an equatorward (poleward) component to the observed (simulated) surface winds and where the observed SAT cooling is strong compared to the simulation (Fig. 5). The second discrepancy is between 150°E and 150°W in JJAS, where the observed response is negative while the simulated response is positive. This again corresponds to an area of opposing SAT responses with an observed warming centered at ~160°E, which would enhance ice melt, as opposed to the weak simulated cooling. An interesting feature of the winter (JJAS) sea ice is that the predominantly zonally symmetric ocean and atmosphere forcings translate to a strong wavenumber-2 response in the simulation and wavenumber-3 response in observations. Whether this is indicative of a mechanism whereby the SAM plays a role in forcing nonannular modes, such as the ACW, remains unclear.

## 5. Discussion and conclusions

The Southern Annular Mode is a pervasive mode of climate variability that affects the atmosphere, ocean, and sea ice at mid and high latitudes over a wide range of time scales. To a good approximation, the SAM is an internal atmospheric mode that produces an integrated response in the high inertia ocean and sea ice systems through surface stresses and via fluxes of heat (and, to a lesser extent, moisture). Here, however, we have also demonstrated that an additional mechanism is at play whereby the ocean feeds back onto the atmosphere, increasing SAT persistence. The SAM is characterized by a highly zonally symmetric response in the atmo-

sphere, particularly away from the surface where topography effects have less influence. However, we have shown that the nonzonal component in the atmosphere plays an important role in explaining the significant regional departures from purely annular responses in the climate system. The following summarizes the response of the CCSM (and, to a large degree, the observed) climate system to a positive phase of the SAM.

When the SAM is in a positive phase, a shifting of atmospheric mass away from the Pole leads to a region of low pressure anomaly over Antarctica that extends to ~55°S with an out of phase circumpolar positive anomaly centered at ~45°S. This pressure difference is associated with a zonal geostrophic wind anomaly that is positive (westerly) south of 45°S and negative (easterly) to the north (Fig. 2). The wind anomaly extends throughout the troposphere and lower stratosphere reaching maximum strength between 200 and 300 mb, straddling the position of the midlatitude jet (Fig. 4a). The wind response represents both a strengthening and a southward shift of the jet (and, more generally, the midlatitude westerlies throughout the column). In the surface boundary layer, drag forces break the geostrophic balance and a meridional wind component (with maximum strength at the surface) results in a poleward flow component south of ~45°S and an equatorward flow to the north (Fig. 4b). This forms a meridional surface convergence–divergence–convergence pattern and consequently a region of subsiding air centered between 40° and 45°S, rising air centered near 60°S but extending south to the Pole, and a weak area of uplift centered between 25° and 30°S (Fig. 4c). With increasing height the wind response becomes increasingly symmetric; however, near the surface there are significant regional departures from the zonal mean response. Of particular importance is an enhanced poleward wind to the west of the Antarctic Peninsula due to the enhanced low pressure system in the Amundsen–Bellinghausen Sea region [which results from the non-axisymmetric distribution of the Antarctic landmass over the South Pole (Lachlan-Cope et al. 2001)] combined with the more localized barrier effect, due to the Antarctic Peninsula (Orr et al. 2004). The SAT response to the SAM (Fig. 5) shows a cooling over much of Antarctica where rising air is associated with adiabatic cooling. An anomalous warming, however, forms over the Antarctic Peninsula region, forced by a conspiring of both zonal advection (of a higher-than-normal climatological zonal temperature gradient) and poleward advection (of the strong meridional temperature gradient in a region of unusually strong poleward air flows). Away from the Antarctic margin and persisting for many months, a feedback response from the

ocean, forced by surface heat fluxes, leads to a residual SAT response that mirrors the persisting SST pattern. Comparing series of uncoupled and coupled GCM experiments from the CSIRO (Mk2) model, Watterson (2000) also demonstrated a modification of lower-tropospheric temperatures in the months after the initial SAM response.

The dynamic response of the ocean to the SAM is essentially immediate with a primarily Ekman-driven transport at shallow depths. The generally southeastward wind stress at all longitudes south of  $\sim 45^{\circ}\text{S}$  results in both an acceleration of the strongly zonal mean flow (near the surface) and an enhancement of the wind-driven northward surface Ekman drift. There is also a poleward movement in the position of maximum zonal and meridional currents (Fig. 8). Farther north the response is an enhanced westerly flow. In line with the wind response forcing, the surface current components show strong zonal symmetry. This circulation response also represents the dominant mode of surface circulation variability (Figs. 1g,h). Although there is an associated redistribution of heat and salt near the surface, these are not sufficiently extensive or of sufficient duration to generate a large zonal flow response through a thermal wind balance. This weak flow is, however, in the same sense as the enhanced zonal Ekman flow while being an order of magnitude smaller (Fig. 9). Extending throughout the water column a small barotropic zonal current is established (Fig. 8). This results from the geostrophic adjustment to the anomalous sea level slope set up by the SAM-induced meridional Ekman transport. A comparison of the associated SAM-driven changes in mass transport through Drake Passage (3.5 Sv) shows good quantitative agreement with observations, 4 Sv (Hughes et al. 2003), based on a one standard deviation SAM response. The convergence of meridional flow near  $45^{\circ}\text{S}$ , with divergent flow to the south and north, creates anomalous vertical motion that extends to depths exceeding 4000 m and acts to significantly enhance the Deacon cell and shift its center southward. Changes to the Deacon cell have the potential to alter intermediate-water transport, and there is some evidence for coherent changes to circulation on intermediate pathways (Fig. 11) where the dominant mode of circulation variability on the  $\sigma_{27.2}$  isopycnal closely matches the corresponding SAM response.

A strong annular SST pattern also builds up in response to the SAM. The large thermal capacity of the mixed layer means that the greatest response lags the atmospheric response by  $\sim 1$  month. The SST response is primarily driven by two forcings. First, the meridional currents advect cold water northward south of  $\sim 45^{\circ}\text{S}$

and warm water southward at midlatitudes north of  $\sim 45^{\circ}\text{S}$  (Fig. 13d). The zonal and vertical heat advection components are significantly smaller than the meridional term. More important, however, is the response of the air-sea heat fluxes, which act to heat and cool the mixed layer. All of the sensible, latent, and net radiative fluxes work in unison to warm the DP region and, in addition, a band centered near  $45^{\circ}\text{S}$  extending from there eastward to Australia (Fig. 14a). The heat flux components also work in concert south of South Africa and to the east of New Zealand. Of major importance to the pattern of heating is the modulating effect of the changing mixed layer depth response, which is strongly related to the overlying wind stresses. The resulting mixed layer temperature tendency due to surface fluxes shows an annular cooling between  $45^{\circ}$  and  $60^{\circ}\text{S}$  (except in the DP region mentioned earlier), warming between  $30^{\circ}$  and  $45^{\circ}\text{S}$ , and general cooling farther north. Importantly, south of  $45^{\circ}\text{S}$  the surface flux and meridional advection terms tend to have an additive cooling effect, which reinforces the oceanic response to the SAM beyond that expected from a simple thermal nondynamic response. Between  $30^{\circ}$  and  $45^{\circ}\text{S}$  the forcings also have an additive warming effect, whereas farther north the meridional advection tends to damp the cooling effect of the surface fluxes. Similar findings are obtained from the zonally averaged results of Watterson (2000) for the CSIRO (Mk2) GCM. Using a slab ocean (i.e., without any ocean dynamics) he finds a temperature dipole straddling  $\sim 30^{\circ}\text{S}$  without a strong high-latitude cooling band. However, with the inclusion of a dynamic ocean, the Ekman-induced heat transport shifts the midlatitude warming northward, cools the high-latitude region, and diminishes the subtropical warming region, consistent with the CCSM heat budget.

Sea ice is affected by the SAM-related modulation of the ocean, wind stresses, and thermal effects. A large component of the immediate ice concentration response at the ice edge is attributable to ice advection alone. Equatorward advection (through the influence of the predominantly north-eastward ocean and sea ice Ekman transport response) tends to increase the ice extent. Zonal advection due to the strengthened westerlies causes both increased ice extent (for example at the Greenwich meridian during summer) and decreased ice extent (for example across the DP region) depending on the orientation of the ice edge to the direction of advection. The ice concentration is also significantly affected in the DP region by the anomalous heating from the increased SAT. Sea ice anomalies are maintained for considerable lengths of time as a result of a positive ice-albedo feedback. A winter SAM event, for instance, while having its greatest sea ice re-

TABLE 3. A comparison between the present study CCSM, reanalysis, and the Hall and Visbeck (2002) climate model atmosphere and ocean variables for annually averaged zonal means and associated regressions (for a 1 std dev positive SAM). High-latitude (H) and low-latitude (L) maximum or minimum values of the annual averages and regressions are shown (in parentheses) for the CCSM and reanalysis (where these exist). The Hall and Visbeck (2002) annual average values are shown at the corresponding regression maximum or minimum and, as a result, cannot be compared directly with the CCSM and reanalysis annual averages shown above.

| Variable                                      | CCSM          |                | Reanalysis     |                | Hall and Visbeck (2002) |                 |
|---|---------------|----------------|----------------|----------------|-------------------------|-----------------|
|   | Zonal mean    | Regression     | Zonal mean     | Regression     | Zonal mean              | Regression      |
| Zonal wind (H) ( $\text{m s}^{-1}$ )          | -5.6 (70.5°S) | 2.0 (57.7°S)   | -2.15 (70.8°S) | 1.35 (60.4°S)  | 3.87                    | 0.57 (55.6°S)   |
| Zonal wind (L) ( $\text{m s}^{-1}$ )          | 9.9 (47.4°S)  | -0.81 (34.3°S) | 6.8 (52.5°S)   | -0.5 (35.9°S)  | 1.4                     | -0.21 (33.3°S)  |
| Meridional wind (H) ( $\text{m s}^{-1}$ )     | 2.9 (71.3°S)  | -0.57 (56°S)   | 1.87 (72°S)    | -0.31 (59°S)   | -0.94                   | -0.16 (55.6°S)  |
| Meridional wind (L) ( $\text{m s}^{-1}$ )     | -2.7 (47.3°S) | 0.23 (34.3°S)  | -1.15 (52.1°S) | 0.13 (35.8°S)  | -0.31                   | 0.07 (33.3°S)   |
| Zonal current (H) ( $\text{cm s}^{-1}$ )      | 16.3 (42.8°S) | 1.12 (56.5°S)  | 12.6 (52.1°S)  | 0.99 (58.2°S)  | —                       | —               |
| Zonal current (L) ( $\text{cm s}^{-1}$ )      | —             | -0.59 (32.3°S) | —              | -0.57 (39.4°S) | —                       | —               |
| Meridional current (H) ( $\text{cm s}^{-1}$ ) | 5.2 (47.6°S)  | 1.12 (58.3°S)  | 4.8 (49.3°S)   | 0.96 (62.2°S)  | 0.68                    | 0.14 (60°S)     |
| Meridional current (L) ( $\text{cm s}^{-1}$ ) | —             | -0.53 (33.5°S) | —              | -0.48 (35.8°S) | 0.127                   | -0.054 (33.3°S) |
| SST (H) ( $^{\circ}\text{C}$ )                | —             | -0.21 (55.7°S) | —              | -0.06 (58.8°S) | 1.84                    | -0.093 (55.6°S) |
| SST (L) ( $^{\circ}\text{C}$ )                | —             | 0.17 (38.6°S)  | —              | 0.057 (39.8°S) | 14.3                    | 0.042 (37.8°S)  |
| DP transport (Sv)                             | 122           | 4              | 130            | 3.5            | 76.1                    | 0.63            |

sponse  $\sim 1$  month after the atmospheric response, shows a significant reemergence of the SAM-induced anomaly the following winter (Fig. 18).

The CCSM simulation shows a remarkable agreement with observations for most of the climate variables discussed. This stems from a very realistic representation of atmospheric variability that is transmitted through to the ocean and ice systems via relatively well-resolved physical processes. Many of the differences in detail can be traced back to the slightly different regional variations in the SAM winds. In particular, the observed response tends to have greater regional departures from the zonal mean, which is potentially a result of the short record length. The major model–observation disagreement involves the SST response. The observed response lacks a distinct annular form and is generally significantly weaker than the simulated response. Again, this may stem from the short observational record and sparse in situ high-latitude measurements rather than model deficiencies. With only three decades of reliable SST reanalysis, the regression of observed SST onto the SAM index is only marginally statistically significant over much of the Southern Ocean.

To summarize the quantitative differences in the SAM on atmosphere and ocean properties, we present a comparison of various annual averaged variables and corresponding SAM anomalies (in the zonal mean) for the CCSM, the observational datasets used in our study, and the Hall and Visbeck (2002) analysis (Table 3). The CCSM wind anomalies are between  $\sim 50\%$  and  $80\%$  greater than the reanalysis anomalies, while the Hall and Visbeck (2002) anomalies are  $\sim 50\%–60\%$

weaker. Much of this can be attributed to the relative sizes of the associated annual-mean wind fields. The CCSM surface circulation anomaly values are in close agreement with the observations, while the Hall and Visbeck (2002) values (meridional component only) are almost an order of magnitude smaller. Again, this appears to be consistent with a much smaller mean-state circulation for the Hall and Visbeck (2002) model (although direct comparison is not possible; see Table 3). The CCSM SST anomalies are considerably greater than the observed SAM SST as a result of the more asymmetric nature of the observed response. The zonally averaged Hall and Visbeck (2002) response does show closer magnitudes to the observations, although this appears to be unrelated to model skill as the response has the same symmetric structure as the CCSM but with smaller magnitudes. Figure 19 shows a schematic depiction of the coupled ocean–atmosphere–ice response to a positive phase of the SAM based on our analysis. While there are substantial differences in the response magnitudes, the mechanisms described here are essentially in agreement with the findings of Hall and Visbeck (2002). Two qualifications should be made, however, in view of our study. (i) There are two major processes increasing the oceanic circumpolar flow during a positive SAM phase. The first is the large increase in the zonal current near the ocean surface as a result of Ekman transport changes and the second is the weak zonal barotropic flow resulting from the geostrophic adjustment to the anomalous sea surface slope. The latter plays the dominant role in increasing the total zonal transport in the ACC. (ii) The sea ice response has significant regional differences with both

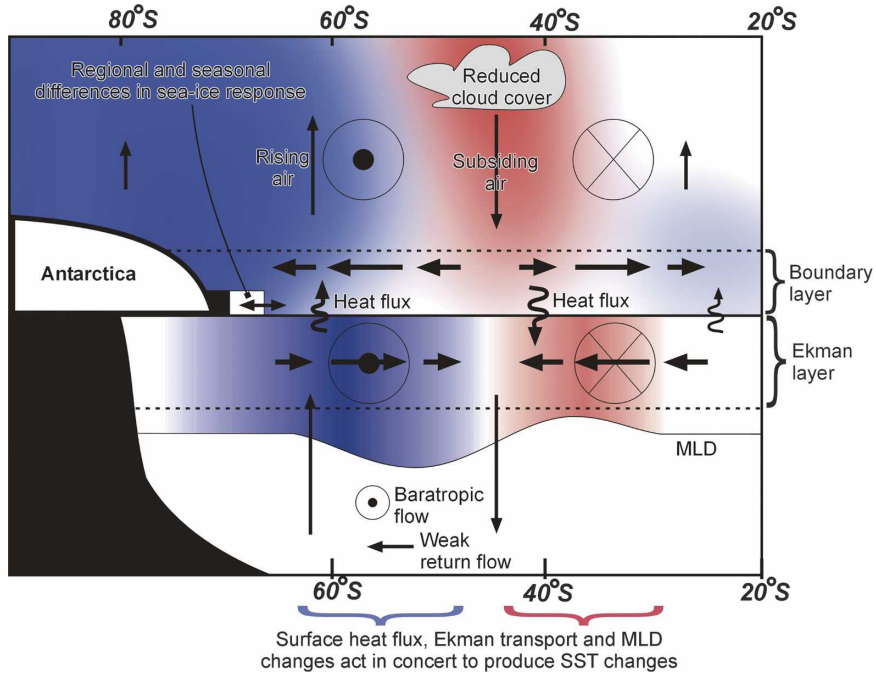


FIG. 19. Schematic representation of the effect on the climate system for a positive SAM. The schematic of circulation, properties, and fluxes for the negative phase of the SAM exhibits the same patterns as displayed above, only with reversed directions of circulation and the opposite sign for property anomalies and fluxes.

increases and decreases in ice extent for a positive phase of the SAM. This results from zonal as well as meridional ice advection responses in combination with thermodynamic processes. The greater zonal symmetry of the Hall and Visbeck (2002) SAM response, together with their ice advection being purely set by oceanic advection, results in a more homogeneous sea ice response than seen in the CCSM or in observations. This is summarized in Fig. 19.

The importance of the climate response to the SAM extends beyond an understanding of climate variability. A number of observational and modeling studies (Gillett and Thompson 2003; Marshall 2003; Thompson and Solomon 2002; Kushner et al. 2001; Thompson and Wallace 2000; Marshall et al. 2004) have demonstrated a positive trend in the SAM index over the past few decades that has been attributed to the depletion of stratospheric ozone and the increase in greenhouse forcing during this period. Marshall et al. (2004) further suggest that it is, in fact, a nonlinear combination of anthropogenic forcing together with natural internal variability that is needed to account for the trend. Both of these mechanisms can act to modify the equator to pole temperature gradient and thus have the potential to enhance the midlatitude jet. Thompson and Solomon (2002) present station and reanalysis results that show a

large fraction of the recent trends in geopotential height, surface wind, and SAT are congruent with the associated SAM trend. For instance, station data is consistent with surface cooling over the bulk of Antarctica, except in the region of the Antarctic Peninsula where there is a warming trend. This has been further associated with a significant retreat in glacier margin positions throughout the peninsula (Cook et al. 2005). Kushner et al. (2001), using the Geophysical Fluid Dynamics Laboratory (GFDL) coupled climate model, find strong similarities between trends in both tropospheric winds and eddy momentum fluxes and the corresponding SAM. However, they find that the trends in atmospheric temperature, at least in a zonal mean sense, cannot be explained by a trend in the SAM alone. Like previous studies, we found that at midlatitudes a shift in the position of the zonal winds is associated with changes in rainfall patterns over Southern Hemisphere continents through changes in cloud cover and moisture advection. Thus, any trend in the SAM may have highly significant impacts on regional rainfall patterns. With such a high proportion of recent trends in SH climate attributable to the SAM, the study of its natural variability provides an important tool to investigate future regional climate change. We have detailed the natural coupled ocean-atmosphere-ice response to

the SAM, as well as the resulting feedbacks between these subcomponents of the climate system. Some of these feedbacks were shown to sustain SAM-induced anomalies over the time scale of seasons to exceeding a year.

**Acknowledgments.** We thank the National Center for Atmospheric Research for providing the CCSM output used in this study. We would also like to thank the three anonymous reviewers for their useful input. This project was supported by the Australian Research Council and the University of New South Wales International Postgraduate Research Scholarship Programme. This work was completed while M. H. England was supported by a CSIRO Flagship Fellowship.

## REFERENCES

- Adler, R., and Coauthors, 2003: The version-2 Global Precipitation Climatology Project (GPCP) monthly precipitation analysis (1979–present). *J. Hydrometeor.*, **4**, 1147–1167.
- Arkin, P. A., and P. Xie, 1996: Analyses of global monthly precipitation using gauge observations, satellite estimates, and numerical model predictions. *J. Climate*, **9**, 840–858.
- Bitz, C. M., and W. H. Lipscomb, 1999: An energy-conserving thermodynamic model of sea ice. *J. Geophys. Res.*, **104**, 15 669–15 677.
- , M. M. Holland, M. Eby, and A. J. Weaver, 2001: Simulating the ice-thickness distribution in a coupled climate model. *J. Geophys. Res.*, **106**, 2441–2463.
- Boer, G. J., S. Fourest, and B. Yu, 2001: The signature of the annular modes in the moisture budget. *J. Climate*, **14**, 3655–3665.
- Brahmananda Rao, V., A. M. C. do Carmo, and S. Franchito, 2003: Interannual variations of storm tracks in the Southern Hemisphere and their connections with the Antarctic Oscillation. *Int. J. Climatol.*, **23**, 1537–1545.
- Branstetter, M. L., and D. J. Erickson III, 2003: Continental runoff dynamics in the Community Climate System Model 2 (CCSM2) control simulation. *J. Geophys. Res.*, **108**, 4550, doi:10.1029/2002JD003212.
- Bromwich, D. H., and R. L. Fogt, 2004: Strong trends in the skill of the ERA-40 and NCEP–NCAR Reanalyses in the high and midlatitudes of the Southern Hemisphere, 1958–2001. *J. Climate*, **17**, 4603–4619.
- Cai, W., and I. G. Watterson, 2002: Modes of interannual variability of the Southern Hemisphere circulation simulated by the CSIRO climate model. *J. Climate*, **15**, 1159–1174.
- , P. H. Whetton, and D. J. Karoly, 2003: The response of the Antarctic Oscillation to increasing and stabilized atmospheric CO<sub>2</sub>. *J. Climate*, **16**, 1525–1538.
- Carril, A. F., and A. Navarra, 2001: The interannual leading modes of the extratropical variability in the Southern Hemisphere simulated by the ECHAM-4 atmospheric model. *Climate Dyn.*, **18**, 1–16.
- Carton, J. A., G. Chepurin, X. Cao, and B. Giese, 2000: A simple ocean data assimilation analysis of the global upper ocean 1950–95. Part I: Methodology. *J. Phys. Oceanogr.*, **30**, 294–309.
- Codron, F., 2005: Relation between annular modes and the mean state: Southern Hemisphere summer. *J. Climate*, **18**, 320–330.
- Collins, W. D., 2001: Parameterization of generalized cloud overlap for radiative calculations in general circulation models. *J. Atmos. Sci.*, **58**, 3224–3242.
- , J. K. Hackney, and D. P. Edwards, 2002: An updated parameterization for infrared emission and absorption by water vapor in the National Center for Atmospheric Research Community Atmosphere Model. *J. Geophys. Res.*, **107**, 4664, doi:10.1029/2001JD001365.
- Cook, A. J., A. J. Fox, D. G. Vaughan, and J. G. Ferrigno, 2005: Retreating glacier fronts on the Antarctic Peninsula over the past half-century. *Science*, **308**, 541–544.
- Fyfe, J. C., G. J. Boer, and G. M. Flato, 1999: The Arctic and Antarctic Oscillations and their projected changes under global warming. *Geophys. Res. Lett.*, **26**, 1601–1604.
- Gent, P. R., and J. C. McWilliams, 1990: Isopycnal mixing in ocean circulation models. *J. Phys. Oceanogr.*, **20**, 150–155.
- Gibson, R., P. Kallberg, and S. Uppala, 1996: The ECMWF re-analysis (ERA) project. *ECMWF Newsletter*, No. 73, ECMWF, Reading, United Kingdom, 7–17.
- Gillet, N. P., and D. W. J. Thompson, 2003: Simulation of recent Southern Hemisphere climate change. *Science*, **302**, 273–275.
- Hall, A., and M. Visbeck, 2002: Synchronous variability in the Southern Hemisphere atmosphere, sea ice, and ocean resulting from the annular mode. *J. Climate*, **15**, 3043–3057.
- Hartmann, D. L., and F. Lo, 1998: Wave-driven zonal flow vacillation in the Southern Hemisphere. *J. Atmos. Sci.*, **55**, 1303–1315.
- Holland, M., 2003: The North Atlantic Oscillation in the CCSM2 and its influence on Arctic climate variability. *J. Climate*, **16**, 2767–2781.
- , C. M. Bitz, and E. Hunke, 2005: Mechanisms forcing an Antarctic dipole in simulated sea ice and surface ocean conditions. *J. Climate*, **18**, 2052–2066.
- Hughes, C. W., P. L. Woodworth, M. P. Meredith, V. Stepanov, T. Whitworth, and A. R. Pyne, 2003: Coherence of Antarctic sea levels, Southern Hemisphere Annular Mode, and flow through Drake Passage. *Geophys. Res. Lett.*, **30**, 1464, doi:10.1029/2003GL017240.
- Hunke, E. C., and J. K. Dukowicz, 1997: An elastic-viscous-plastic model for sea ice dynamics. *J. Phys. Oceanogr.*, **27**, 1849–1867.
- Kalnay, E., and Coauthors, 1996: The NCEP/NCAR 40-Year Reanalysis Project. *Bull. Amer. Meteor. Soc.*, **77**, 437–471.
- Karoly, D. J., 1990: The role of transient eddies in low-frequency zonal variations of the Southern Hemisphere circulation. *Tellus*, **42A**, 41–50.
- Kiehl, J. T., and P. R. Gent, 2004: The Community Climate System Model, version 2. *J. Climate*, **17**, 3666–3682.
- Kushner, P. J., I. M. Held, and T. L. Delworth, 2001: Southern Hemisphere atmospheric circulation response to global warming. *J. Climate*, **14**, 2238–2249.
- Lachlan-Cope, T. A., W. M. Connolley, and J. Turner, 2001: The role of the non-axisymmetric Antarctic orography in forcing the observed pattern of variability of the Antarctic climate. *Geophys. Res. Lett.*, **28**, 4111, doi:10.1029/2001GL013465.
- Large, W. G., J. C. McWilliams, and S. C. Doney, 1994: Oceanic vertical mixing: A review and a model with a nonlocal boundary layer parameterization. *Rev. Geophys.*, **32**, 363–403.
- Lefebvre, W., H. Goosse, R. Timmermann, and T. Fichefet, 2004: Influence of the Southern Annular Mode on the sea ice–

- ocean system. *J. Geophys. Res.*, **109**, C09005, doi:10.1029/2004JC002403.
- Limpasuvan, V., and D. L. Hartmann, 2000: Wave-maintained annular modes of climate variability. *J. Climate*, **13**, 4414–4429.
- Liu, J., J. A. Curry, and D. G. Martinson, 2004: Interpretation of recent Antarctic sea ice variability. *Geophys. Res. Lett.*, **31**, L02205, doi:10.1029/2003GL018732.
- Lorenz, D. J., and D. L. Hartmann, 2001: Eddy-zonal flow feedback in the Southern Hemisphere. *J. Atmos. Sci.*, **58**, 3312–3327.
- Lovenduski, N., and N. Gruber, 2005: Impact of the Southern Annular Mode on Southern Ocean circulation and biology. *Geophys. Res. Lett.*, **32**, L11603, doi:10.1029/2005GL022727.
- Marshall, G. J., 2003: Trends in the Southern Annular Mode from observations and reanalyses. *J. Climate*, **16**, 4134–4143.
- , P. A. Stott, J. Turner, W. M. Connolley, J. C. King, and T. A. Lachlan-Cope, 2004: Causes of exceptional atmospheric circulation changes in the Southern Hemisphere. *Geophys. Res. Lett.*, **31**, L14205, doi:10.1029/2004GL019952.
- McDougall, T. J., D. R. Jckett, D. G. Wright, and R. Feistel, 2003: Accurate and computationally efficient algorithms for potential temperature and density of seawater. *J. Atmos. Oceanic Technol.*, **20**, 730–741.
- Meredith, M. P., P. L. Woodworth, C. W. Hughes, and V. N. Stepanov, 2004: Changes in the ocean transport through Drake Passage during the 1980s and 1990s, forced by changes in the Southern Annular Mode. *Geophys. Res. Lett.*, **31**, L21305, doi:10.1029/2004GL021169.
- Mo, K. C., 2000: Relationships between low-frequency variability in the Southern Hemisphere and sea surface temperature anomalies. *J. Climate*, **13**, 3599–3610.
- North, G. R., T. L. Bell, R. F. Cahalan, and F. G. Moeng, 1982: Sampling errors in the estimation of empirical orthogonal functions. *Mon. Wea. Rev.*, **110**, 699–706.
- Oke, P. R., and M. H. England, 2004: Oceanic response to changes in the latitude of the Southern Hemisphere subpolar westerly winds. *J. Climate*, **17**, 1040–1054.
- Orr, A., D. Cresswell, G. J. Marshall, J. C. R. Hunt, J. Sommeria, C. G. Wang, and M. Light, 2004: A ‘low-level’ explanation for the recent large warming trend over the western Antarctic Peninsula involving blocked winds and changes in zonal circulation. *Geophys. Res. Lett.*, **31**, L06204, doi:10.1029/2003GL019160.
- Rasch, P. J., and J. E. Kristjansson, 1998: A comparison of the CCM3 model climate using diagnosed and predicted condensate parameterizations. *J. Climate*, **11**, 1587–1614.
- Rayner, N. A., D. E. Parker, E. B. Horton, C. K. Folland, L. V. Alexander, D. P. Rowell, E. C. Kent, and A. Kaplan, 2003: Global analyses of sea surface temperature, sea ice, and night marine air temperature since the late nineteenth century. *J. Geophys. Res.*, **108**, 4407, doi:10.1029/2002JD002670.
- Reynolds, R. W., N. A. Rayner, T. M. Smith, D. C. Stokes, and W. Wang, 2002: An improved in situ and satellite SST analysis for climate. *J. Climate*, **15**, 1609–1625.
- Rintoul, S., and M. H. England, 2002: Ekman transport dominates air-sea fluxes in driving variability of subantarctic mode water. *J. Phys. Oceanogr.*, **32**, 1308–1321.
- Robinson, W. A., 1991: The dynamics of the zonal index in a simple model of the atmosphere. *Tellus*, **43A**, 295–305.
- Santoso, A., and M. H. England, 2004: Antarctic Intermediate Water variability in a coupled climate model. *J. Phys. Oceanogr.*, **34**, 2160–2179.
- Sciremmanno, F., Jr., 1979: A suggestion for the presentation of correlations and their significance levels. *J. Phys. Oceanogr.*, **9**, 1273–1276.
- Sexton, D. M. H., 2001: The effect of stratospheric ozone depletion on the phase of the Antarctic Oscillation. *Geophys. Res. Lett.*, **28**, 3697–3700.
- Silvestri, G. E., and C. S. Vera, 2003: Antarctic Oscillation signal on precipitation anomalies over southeastern South America. *Geophys. Res. Lett.*, **30**, 2115, doi:10.1029/2003GL018277.
- Smith, R. D., and J. C. McWilliams, 2003: Anisotropic horizontal viscosity for ocean models. *Ocean Model.*, **5**, 129–156.
- Thompson, D. W. J., and J. M. Wallace, 2000: Annular modes in the extratropical circulation. Part I: Month-to-month variability. *J. Climate*, **13**, 1000–1016.
- , and S. Solomon, 2002: Interpretation of recent Southern Hemisphere climate change. *Science*, **296**, 895–899.
- Turner, J., 2004: The El Niño–Southern Oscillation and Antarctica. *Int. J. Climatol.*, **24**, 1–31.
- Visbeck, M., and A. Hall, 2004: Reply. *J. Climate*, **17**, 2255–2258.
- Watterson, I. G., 2000: Southern midlatitude zonal wind vacillation and its interaction with the ocean in GCM simulations. *J. Climate*, **13**, 562–578.
- White, W. B., 2004: Comments on “Synchronous variability in the Southern Hemisphere atmosphere, sea ice, and ocean resulting from the annular mode.” *J. Climate*, **17**, 2249–2254.
- Yuan, X., and D. G. Martinson, 2001: The Antarctic Dipole and its predictability. *Geophys. Res. Lett.*, **28**, 3609–3612.
- Zhou, T., and R. Yu, 2004: Sea-surface temperature induced variability of the Southern Annular Mode in an atmospheric general circulation model. *Geophys. Res. Lett.*, **31**, L24206, doi:10.1029/2004GL021473.